

# LLE Review

## Quarterly Report



**July–September 1991**

Laboratory for Laser Energetics  
College of Engineering and Applied Science  
University of Rochester  
250 East River Road  
Rochester, New York 14623-1299



This report was prepared as an account of work conducted by the Laboratory for Laser Energetics and sponsored by New York State Energy Research and Development Authority, the University of Rochester, the U.S. Department of Energy, and other agencies.

Neither the above-named sponsors, nor any of their employees, makes any warranty, expressed or implied, or assumes any legal liability or responsibility for the accuracy, completeness, or usefulness of any information, apparatus, product, or process disclosed, or represents that its use would not infringe privately owned rights.

Reference herein to any specific commercial product, process, or service by trade name, mark, manufacturer, or otherwise, does not necessarily constitute or imply its endorsement, recommendation, or favoring by the United States Government or any agency thereof or any other sponsor.

Results reported in the LLE Review should not be taken as necessarily final results as they represent active research. The views and opinions of authors expressed herein do not necessarily state or reflect those of any of the above sponsoring entities.

# Section 1

## PROGRESS IN LASER FUSION

### 1.A Results of Imploding-Target Burnthrough Experiments Using SSD Smoothing

Illumination uniformity is important for the success of inertial confinement fusion (ICF).<sup>1</sup> One potentially serious consequence of drive nonuniformity in direct-drive ICF experiments is the development of the Rayleigh-Taylor (RT) instability,<sup>2</sup> which can adversely affect target performance through mixing. Such mixing was assumed to be responsible for the discrepancy between the experimental and simulation results of the burnthrough experiments reported in Ref. 3. In those experiments, the laser irradiated a spherical target that consisted of a glass shell or a solid glass sphere overcoated with a parylene [or polyparaxylylene, (CH)<sub>x</sub>] layer, in which one or more thin signature layers of moderate- to high-Z material were embedded for diagnostic purposes to signal the penetration of the heat front. Two potential regions for growth of the RT instability exist in such targets, one at the ablation surface and one at the parylene-signature-layer interface. Under current laser conditions, the instability grows from initial perturbations created mainly by the laser illumination nonuniformity, although normal target fabrication imperfections also play a minor role in initializing the instability. As laser uniformity improvements continue to be made, the contribution of these target imperfections will become more significant.

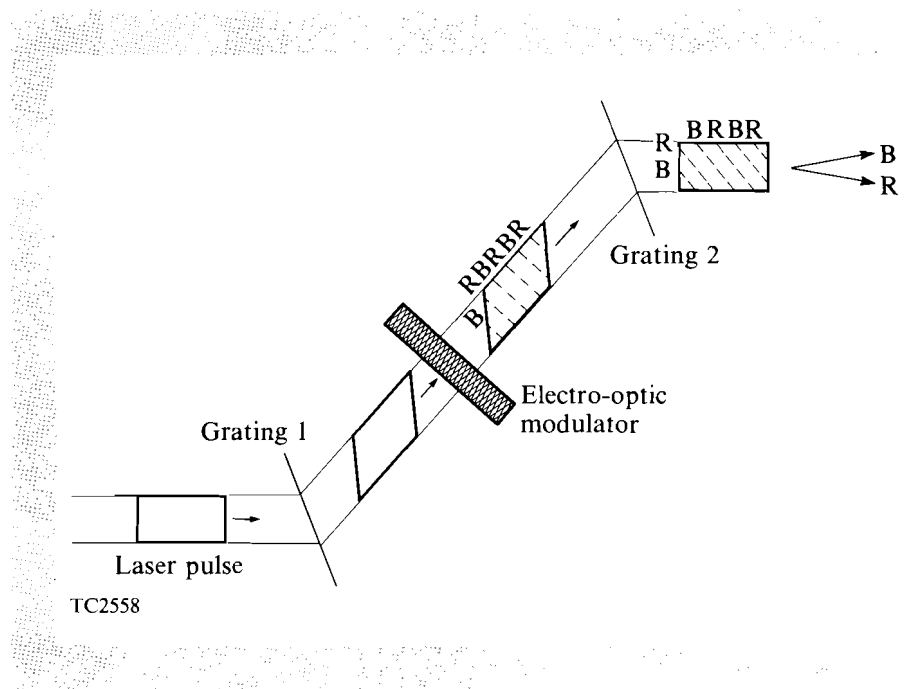
A primary result of the analysis in Ref. 3 was that the timing of the burnthrough was correlated with the illumination nonuniformity. This is based on the conclusion that mixing from a rapidly growing unstable region leads to an early burnthrough time. For similar shell drive conditions

(acceleration, mass-density scale length, and Atwood number), the RT growth rates should be similar and the rms amplitude of the instability should depend on the initial perturbation as long as the instability has not saturated. Thus, a conclusion of Ref. 3 was that the effectiveness of new methods developed to improve the laser illumination could be tested by measuring the burnthrough time in burnthrough targets, along with other observables affected by mixing, such as neutron yield and fuel density.

Since the data presented in Ref. 3 were collected, a number of improvements to the 351-nm irradiation uniformity of the 24-beam OMEGA laser system have been implemented, including the use of distributed phase plates (DPP's)<sup>4,5</sup> and of smoothing by spectral dispersion (SSD).<sup>6</sup> In the SSD technique currently installed on OMEGA, a spectrally dispersed, broad-bandwidth, phase-modulated laser pulse is produced by an electro-optic phase modulator and a pair of transmission gratings, as shown in Fig. 48.1. When this pulse is focused onto the target through a DPP and a lens, the instantaneous speckle pattern formed on target by the DPP will vary rapidly as the red- and blue-shifted components cycle across the beam, resulting in an extremely uniform, time-averaged, far-field profile. The larger the bandwidth, the more rapidly the structure changes in time and achieves a given level of smoothing. This is illustrated in Figs. 48.2(a) and 48.2(b) where we have plotted the predicted rms on-target nonuniformity for various  $\ell$ -mode ranges as a function of averaging time for two different bandwidths:  $\Delta\lambda/\lambda = 5 \times 10^{-5}$  and  $\Delta\lambda/\lambda = 3 \times 10^{-4}$ . The initial  $\ell$ -mode spectrum was the same in each case and was derived from measured-beam, far-field profiles. The effect of thermal smoothing has been included by multiplying the amplitude of each  $\ell$ -mode by a factor  $\exp(-0.01\ell)$ , in accordance with the

Fig. 48.1

A schematic of SSD as implemented on the OMEGA laser system. A spectrally dispersed broad-bandwidth, phase-modulated pulse is produced by the electro-optic modulator and the pair of transmission gratings. R and B refer to the red- and blue-shifted components of the beam.



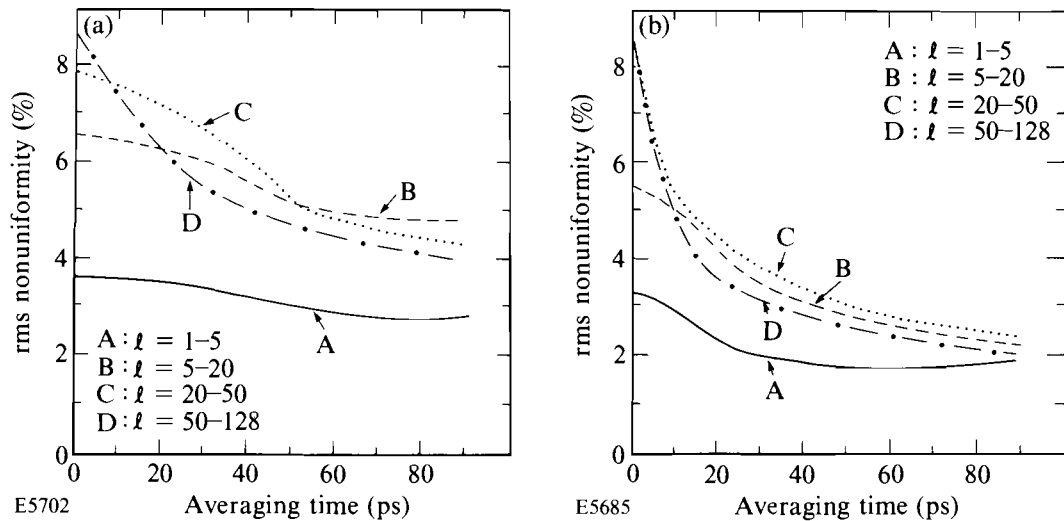


Fig. 48.2

Illumination rms nonuniformity on target for various  $\ell$ -mode ranges as a function of averaging time for SSD bandwidths of (a)  $\Delta\lambda/\lambda = 5 \times 10^{-5}$  and (b)  $\Delta\lambda/\lambda = 3 \times 10^{-4}$ . The modulation frequency was 8 GHz. In each case a thermal smoothing factor of 1% was assumed.

“cloudy-day” model.<sup>7</sup> By comparing the two figures it can be seen that the overall level of nonuniformity is expected to fall more quickly and to a lower asymptotic value in the higher bandwidth case than in the lower. It is also noteworthy that this effect is much more pronounced for the higher  $\ell$ -modes, which are predicted to be the more destructive ones in terms of causing early burnthrough.<sup>3</sup>

In this article, we present results of burnthrough experiments undertaken to study the effect of the SSD bandwidth on both the burnthrough time and on the neutron yield of  $D_2$ -filled imploding targets. We observe that increasing the SSD bandwidth from zero to  $\Delta\lambda/\lambda = 4 \times 10^{-4}$  increases the burnthrough time by about 200 ps. Based on simulations carried out on the one-dimensional (1-D) code *LILAC* and a mixing model postprocessor, we attribute these improvements to a decrease, as a result of SSD, in the amplitude of the initial perturbations that seed the RT instability.

The experiments were carried out on the OMEGA laser system at 351 nm with 600-ps FWHM Gaussian pulses at peak intensities of about  $8-9 \times 10^{14}$  W/cm<sup>2</sup>. DPP's were used throughout the experiment along with values for the SSD bandwidth ranging from  $\Delta\lambda/\lambda = 0-4 \times 10^{-4}$ . In all cases the SSD modulation frequency was 8.74 GHz. The targets consisted of 3- $\mu$ m-thick glass shells with diameters ranging from 260  $\mu$ m to 270  $\mu$ m, filled with

50 atm of  $D_2$  and coated with  $6\ \mu\text{m}$  of parylene. The parylene layer was chosen to be slightly larger than the computed 1-D burnthrough depth in order to give maximum sensitivity to changes in drive uniformity. A barrier layer, consisting of  $0.1\ \mu\text{m}$  of Al, was deposited on the targets to prevent shinethrough<sup>8</sup> of the early part of the laser pulse into the target before formation of the critical surface. X-ray emission from the barrier layers also served as a timing marker since a fiducial beam was not available for these experiments. Illumination uniformity and absorption were optimized by choosing targets with diameters about a factor of 1.28 smaller than the diameter of the first zero of the DPP point spread function ( $387\ \mu\text{m}$ ). Targets with such diameters intercept 81.5% of the beam energy.

Measurements of the temporal emission of the Al and Si H-like and He-like lines were provided by SPEAXS,<sup>9</sup> a time-resolving x-ray spectrometer in which an elliptically curved pentaerythritol (PET) crystal analyzer is used to disperse the x-ray spectrum (1.5- to 2.5-keV range) onto the slit of an x-ray streak camera. Neutron yields from the DD fusion reactions were measured using silver activation and a set of scintillator/photomultiplier pairs.<sup>10,11</sup> Figure 48.3 shows a typical SPEAXS spectrum containing K-shell emission from both the Al barrier layer and the glass signature layer. Lineouts along the time axis for both the Al and Si H-like 1s-3p lines are shown in Fig. 48.4. In view of the lack of an absolute laser timing fiducial

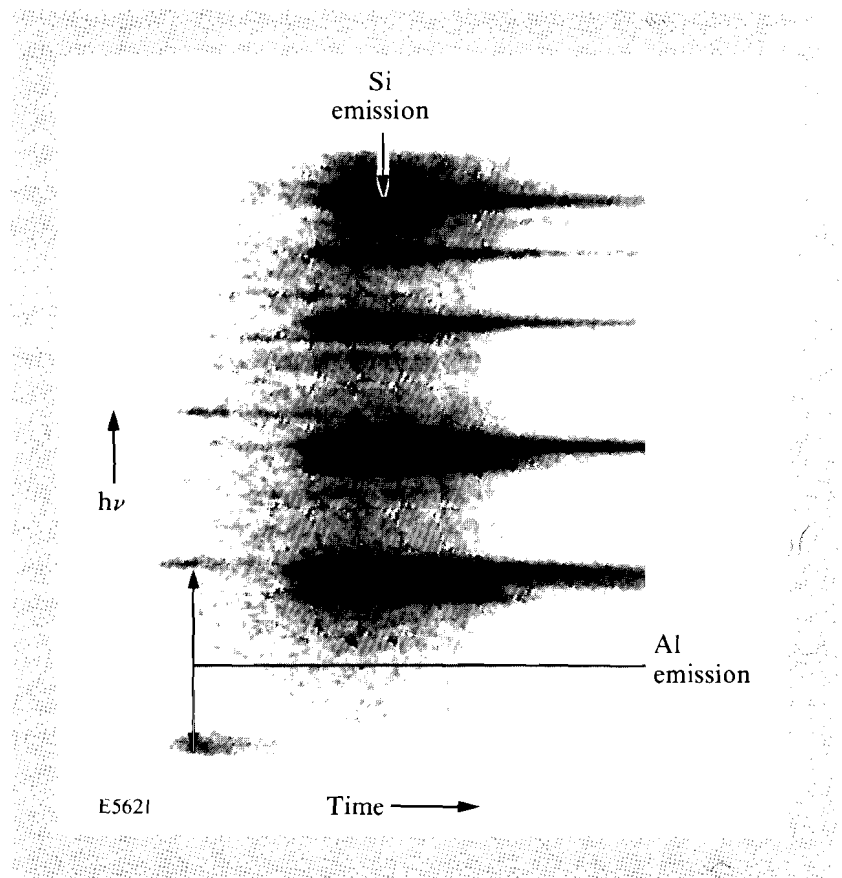


Fig. 48.3  
Typical SPEAXS spectrum showing emission from both the outer Al layer and the glass signature layer (Si emission).

during these experiments and since for the purposes of this article we are only interested in relative measurements, we have defined the burnthrough time as the temporal difference between the onset of the Al and Si emission. (The onset is defined as the time at which the emission reaches 1/10 of its maximum value.) Data recorded on previous experiments, when a timing fiducial was present, would indicate that the Al onset time is  $\sim 600$  ps before the peak of the laser pulse.

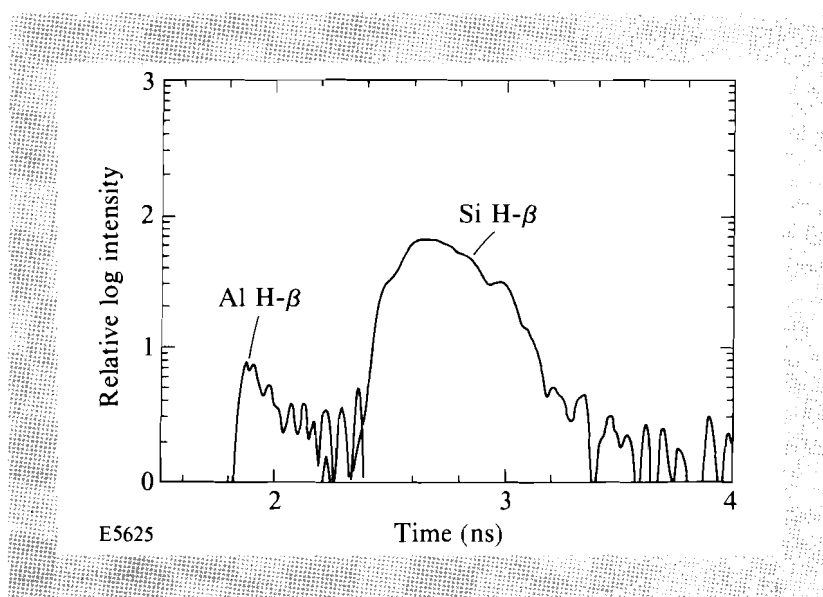
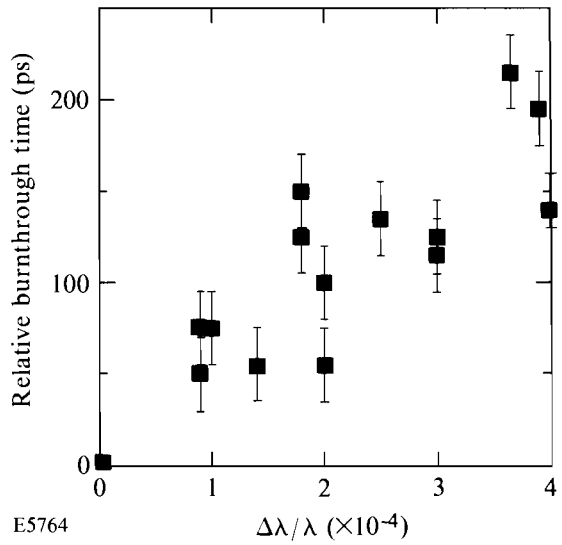


Fig. 48.4  
Temporal lineouts of the Al and Si H-like 1s-3p lines. The choice of the zero point on the time axis is arbitrary.

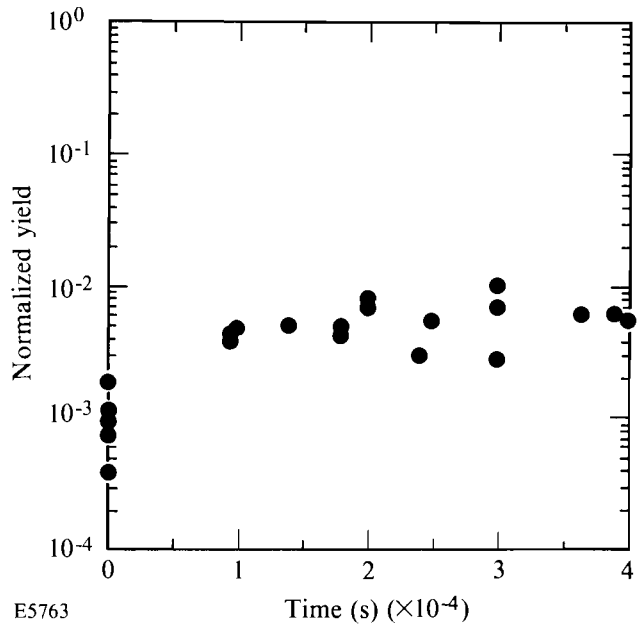
Figure 48.5 shows the measured relative burnthrough times for several series of target shots with SSD bandwidths ranging from  $\Delta\lambda/\lambda = 0-4 \times 10^{-4}$ . For the purposes of comparing data from several different shot series on the same graph, each with slightly different initial conditions, the burnthrough time at zero bandwidth has been defined as 0 ps for each series. Actual zero bandwidth time delays were typically  $\sim 550$  ps between Al and Si emission, i.e., Si onset times were typically  $\sim 50$  ps before peak laser power. There are two things to note from Fig. 48.5: (a) for all shot series we have always seen an improvement in burnthrough time when SSD bandwidth is present, compared to zero bandwidth shots, and (b) the burnthrough times continue to improve as SSD bandwidth is increased, with up to a 200-ps improvement at the maximum measured bandwidth of  $4 \times 10^{-4}$ . Figure 48.6 shows the measured neutron yield, expressed as a fraction of the 1-D yield predicted by *LILAC*, as a function of SSD bandwidth. In this case there is still a noticeable and consistent improvement when bandwidth is present, compared to shots without SSD. However, there is not as clear a trend of improving yield with increasing bandwidth as with the burnthrough times, indicating that the neutron yield is not as sensitive an indicator of illumination uniformity as the burnthrough measurement. This is consistent with the idea that, whereas the burnthrough time is sensitive to instabilities that develop during the acceleration phase of the implosion, the neutron yield, which occurs much later during the implosion, has the potential to be affected by many more physical

Fig. 48.5  
 Relative burnthrough times plotted as a function of SSD bandwidth. For each sequence of shots the zero-bandwidth case has been normalized to 0 ps to allow a comparison to be made.



processes, including additional fluid instabilities that can develop during the deceleration phase. Even at a bandwidth of  $4 \times 10^{-4}$  we still observe burnthrough into the glass layer shortly after the peak of the laser pulse, indicating that a substantial degree of mix has already occurred.

Fig. 48.6  
 Normalized neutron yields for the data in Fig. 48.5 plotted as a function of SSD bandwidth. The normalized yield is expressed in terms of the ratio of the measured yield to the 1-D yield predicted by *LILAC*.



The effect of SSD on the burnthrough time can be analyzed theoretically with the 1-D hydrodynamic code *LILAC* and a post-processor that models the evolution of the RT instability<sup>3</sup> and calculates a mixing thickness. For targets consisting of a parylene-coated glass shell we need to consider only the RT growth at the ablation surface. The growth rate at the glass-parylene interface is smaller than at the ablation surface because of the low Atwood number.<sup>3</sup> Burnthrough time is defined in the model as the time at which the mixing thickness is larger than the distance between the 200-eV isotherm and the glass-parylene interface. The mix thickness is calculated using a multi-mode analysis<sup>12</sup> in which each mode of an initial perturbation spectrum is evolved exponentially with a given growth rate. The analysis also includes a saturation model. The growth rate for the ablation-surface instability is stabilized by the ablation process and is expressed as<sup>13</sup>  $\gamma = \alpha\sqrt{ka} - \beta kV_a$ , where  $k$  is the unstable mode wave number,  $a$  is the acceleration, and  $V_a$  is the ablation velocity. The constant values  $\alpha = 0.9$  and  $\beta = 3-4$  provide a good fit to the growth rates obtained from full two-dimensional simulations. Further details on the model can be found in Ref. 3.

The main effect of SSD is to modify the initial perturbation spectrum. As can be seen from Fig. 48.2, SSD reduces the smoothing time and also smooths out the higher  $\ell$ -modes faster and more efficiently than the lower  $\ell$ -modes. The temporal effect of SSD is too complex to be included into the mix model. Instead, we will show that the reduction of the higher  $\ell$ -mode amplitude in the initial perturbation spectrum leads to a reduction in the mix thickness, which in turn increases the burnthrough time. In Fig. 48.2 the rms perturbation is given as a percentage of the beam laser energy on target. The mixing post-processor, however, requires an initial perturbation of the target surface. We have at this point no way to calculate either the rms surface perturbations from a given illumination rms perturbation or the surface perturbation that will yield the hydrodynamic behavior equivalent to a given illumination perturbation. For the purpose of this article we assume that the illumination perturbation produces an equivalent surface perturbation, or at least, that the surface perturbation is proportional to the illumination perturbation. A more complex relationship between the illumination perturbation and the surface perturbation would only change the parameters in the initial perturbation spectrum, but not the conclusion of the analysis.

Initial perturbation spectra for the zero-bandwidth case and the maximum-bandwidth case were constructed partly from a sum of two exponential functions so as to approximate the measured irradiation uniformity on target.<sup>14</sup> The published spectra were generated only to  $\ell = 64$ . The constructed spectra are given by  $A_{\ell,m}(t=0) = \xi_0[\exp(-S_1\ell) + R_2 \exp(-S_2\ell)]$  ( $\mu\text{m}/\text{mode}$ ) and  $A_{\ell,m} = A_{35,m}$  for  $35 < \ell < 64$ , where  $\xi_0$  is the initial perturbation in  $\mu\text{m}$ ,  $\ell$  is the Legendre mode number,  $S_1$  and  $S_2$  are chosen to obtain the required rms nonuniformity, and  $R_2 = \exp[(S_2 - S_1)\ell_0]$ , with  $\ell_0$  set for a given spectrum. This formalism provides flexibility and a description of the initial perturbation that depends on one parameter  $\xi_0$ . (The modes are assumed to be symmetric in the azimuthal direction.) Appropriate values for  $S_1$ ,  $S_2$ , and  $\ell_0$  are, for zero bandwidth,  $S_1 = 0.13$ ,  $S_2 = -0.039$ , and  $\ell_0 = 17$ ;

for full bandwidth,  $S_1 = 0.20$ ,  $S_2 = 0.0$ , and  $\ell_o = 17$ . The constructed spectra need to be extended to  $\ell = 200$  in order to include the fastest growing modes near  $\ell = 100$ . Assuming the same 1% thermal smoothing by the target as in Fig. 48.2, the extended spectra were given the form  $\exp(-0.01\ell)$  for  $64 < \ell < 200$ . Figure 48.7 shows the constructed initial spectrum for the zero-bandwidth (curve a) and the full-bandwidth (curve b) cases for the same initial amplitude  $\xi_o$ . The effect of SSD is to reduce the rms nonuniformity mainly for modes above about  $\ell = 10$ .

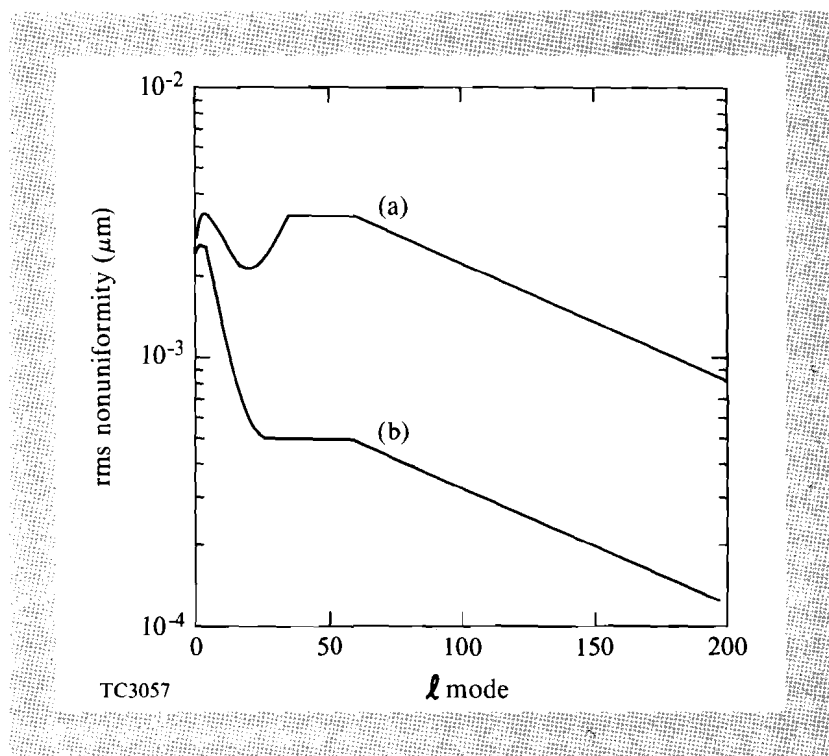


Fig. 48.7

$\ell$ -mode distribution of the initial perturbation used in the model to estimate the mixing-region thickness. Curve (a) is for zero bandwidth and curve (b) is for the maximum bandwidth case ( $\Delta\lambda/\lambda = 4 \times 10^{-4}$ ).

The value of  $\xi_o$  is chosen such that the computed delay between the onset of the Si and Al emission is approximately equal to the measured time delay for the zero-bandwidth case. Because of the lack of a timing fiducial in the measurements, a comparison of absolute burnthrough times between the experiment and the simulation is not possible. Also, the resonance line emission from the Al barrier layer cannot be used for a precise timing comparison because the computed temporal emission from *LILAC* depends on the laser pulse shape early in time, which is not known accurately. Since we want to show only the relative effect of decreasing the initial perturbation, an absolute timing comparison is not necessary; however, the computed burnthrough times still need to be realistic in order to make the argument credible. Based on previous measurements of the Al barrier-layer emission in which a timing fiducial was present, we assume that the Al emission occurs 600 ps before the peak of the pulse.

The effect of SSD on the burnthrough times can be observed in simulations of the targets previously described. Using the zero-bandwidth spectrum

in Fig. 48.7 (curve a), a value for  $\xi_0 = 350 \text{ \AA}$  gives a burnthrough time of about  $-65 \text{ ps}$  with respect to the peak of the laser pulse, approximately the time measured in the experiment. Using the maximum-bandwidth spectrum in Fig. 48.7 (curve b) and the same value for  $\xi_0$  gives a burnthrough time of  $+95 \text{ ps}$ . Thus, when SSD is added to the mix model, keeping the initial perturbation amplitude constant, the burnthrough time is advanced by  $160 \text{ ps}$ . This value agrees reasonably well with the  $200\text{-ps}$  time delay between the zero-bandwidth and the maximum-bandwidth burnthrough times measured in the experiment. Therefore, within the limitations of modeling the initial perturbation in the mix model, we have shown that improving the illumination uniformity with SSD in the mix model, through the reduction in the amplitude of modes  $\ell > 10$ , accounts for the observed increase in the burnthrough time. Also, the analysis confirms that the evolution of the instability remains mostly linear as defined in Ref. 12.

In summary, we have investigated the effect of the drive-uniformity improvements resulting from SSD in burnthrough experiments. We had shown in previous work that the burnthrough time is a measure of the evolution of the RT instability at the ablation surface and the glass-parylene interface. Since the evolution does not saturate it depends on the initial perturbation and should, therefore, be sensitive to the level of illumination nonuniformity. The measured burnthrough times show continued improvement as the SSD bandwidth is increased from zero to  $\Delta\lambda/\lambda = 4 \times 10^{-4}$ , consistent with a continually improving uniformity. The neutron yields show an immediate improvement with a small amount of SSD bandwidth present, but do not show a strong bandwidth dependence beyond that. The measured improvements in burnthrough times can be reproduced by a post-processor to the 1-D code *LILAC* that models the evolution of the RT instability and includes initial perturbation spectra consistent with the measured change in uniformity.

#### ACKNOWLEDGMENT

The authors would like to thank S. Skupsky for providing the irradiation uniformity data and for many useful discussions, the target fabrication group, and the members of the OMEGA laser and experimental operations groups. This work was supported by the U.S. Department of Energy Office of Inertial Confinement Fusion under agreement No. DE-FC03-85DP40200 and by the Laser Fusion Feasibility Project at the Laboratory for Laser Energetics, which is sponsored by the New York State Energy Research and Development Authority and the University of Rochester.

#### REFERENCES

1. J. Nuckolls *et al.*, *Nature* **239**, 139 (1972).
2. S. Chandrasekhar, *Hydrodynamic and Hydromagnetic Stability* (Clarendon Press, Oxford, England, 1961), Chap. 10.
3. J. Deletrez, D. K. Bradley, P. A. Jaanimagi, and C. P. Verdon, *Phys. Rev. A* **41**, 5583 (1990).
4. Y. Kato *et al.*, *Phys. Rev. Lett.* **53**, 1057 (1984).
5. LLE Review **33**, 1 (1987).

6. S. Skupsky, R. W. Short, T. Kessler, R. S. Craxton, S. Letzring, and J. M. Soures, *J. Appl. Phys.* **66**, 3456 (1989).
7. S. E. Bodner, *J. Fusion Energy* **1**, 221 (1981).
8. D. K. Bradley, T. Boehly, D. L. Brown, J. Delettrez, W. Seka, and D. Smith, in *Laser Interaction and Related Plasma Phenomena*, edited by H. Hora and G. H. Miley (Plenum Press, New York, 1991), Vol. 9, pp. 323–334.
9. B. L. Henke and P. A. Jaanimagi, *Rev. Sci. Instrum.* **56**, 1537 (1985).
10. LLE Review **36**, 150 (1988).
11. M. C. Richardson, R. L. Keck, S. A. Letzring, R. L. McCrory, P. W. McKenty, D. M. Roback, J. M. Soures, C. P. Verdon, S. M. Lane, and S. G. Prussin, *Rev. Sci. Instrum.* **57**, 1737 (1986).
12. S. W. Haan, *Phys. Rev. A* **39**, 5812 (1989).
13. H. Takabe *et al.*, *Phys. Fluids* **28**, 3676 (1985).
14. R. L. McCrory, J. M. Soures, C. P. Verdon, S. Skupsky, T. J. Kessler, S. A. Letzring, W. Seka, R. S. Craxton, R. Short, P. A. Jaanimagi, M. Skeldon, D. K. Bradley, J. Delettrez, R. L. Keck, H. Kim, J. P. Knauer, R. L. Kremens, and F. J. Marshall, *Plasma Physics and Controlled Fusion* **31**, 1517 (1989).

## 1.B A Practical Nonlocal Model for Electron Heat Transport in Laser Plasmas

Computer simulations of electron heat transport, using the Fokker-Planck (FP) equation under conditions relevant to inertial-confinement fusion (ICF), have revealed inadequacies in the classical heat-flow model  $\mathbf{q}_{SH} = -\kappa_{SH}\nabla T$  (where  $\kappa_{SH}$  is the Spitzer-Härm heat coefficient and  $T$  is the electron temperature in energy units).<sup>1,2</sup> These inadequacies appear in the form of excessive heat flux under sharp temperature gradients, and in the lack of preheat due to long mean-free-path electrons ahead of the main heat front. Although the first inadequacy has been overcome to some extent with the use of flux limiters,<sup>3</sup> there are cases, for example involving thermal smoothing,<sup>2</sup> when flux limiting is totally ineffective. As for the second inadequacy, in order to properly account for preheat phenomena, one has to resort to more sophisticated nonlocal heat-transport models, such as the FP equation or convolution formulas.

The use of convolution techniques has been suggested as a simpler, and computationally more efficient, alternative to solving the full FP equation for the electrons.<sup>4–13</sup> The basic principle behind this approach is to convolve the

local heat flux  $q_{SH}$  with some appropriate kernel in configuration space so as to obtain (to some degree of approximation) the more accurate FP heat flow  $q_{FP}$ . The first practical convolution formula (also known as nonlocal heat-flow formula) was proposed by Luciani, Mora, and Virmont<sup>5</sup>

$$q_{LMV}(x) = \int_{-\infty}^{\infty} dx' \frac{q_{SH}(x')}{2a\lambda_e(x')} \exp[-\theta(x, x')] \quad 1(a)$$

where

$$\theta(x, x') = \left| \frac{1}{a\lambda_e(x')n(x')} \int_{x'}^x dx'' n(x'') \right| \quad 1(b)$$

is the number of stopping lengths between  $x$  and  $x'$  (sometimes referred to as optical depth) of an electron of temperature  $T(x')$ ,  $\lambda_e = T^2/4\pi n e^4 (Z+1)^{1/2} \ln \Lambda$  is its stopping length, and  $a$  is a free parameter. Here, the Coulomb logarithm (assumed the same for electrons and ions) is denoted by  $\ln \Lambda$ ,  $n$  is the electron number density,  $e$  is the electronic charge, and  $Z$  is the ionic charge number. Despite the fact that this formula (referred to from now on as LMV) was not originally derived from first principles, it does have certain desirable properties: it gives flux inhibition under sharp temperature gradients, it can predict preheat ahead of the main heat front, and it yields the classical result in the collisional limit. Several subsequent papers by the same and other authors have attempted to justify and improve upon the LMV model.<sup>7,8</sup> Using a different approach, Albritton, Williams, Bernstein, and Swartz derived a more complicated formula by directly solving a simplified form of the FP equation. Their model (to be referred as AWBS) has likewise been improved upon by others.<sup>9,10</sup>

Despite the success of most nonlocal formulas in modeling heat transport under idealized laser-fusion conditions (i.e., with no hydrodynamics and high initial temperatures), to the best of our knowledge there have been no comparisons made with FP simulations under realistic ICF conditions, where a fuel pellet is imploded under laser irradiation. Moreover, Prasad and Kershaw<sup>11</sup> have recently suggested that there may be inherent numerical difficulties associated with the implementation of certain nonlocal models in hydrodynamic codes.

The aim of this article is to give a brief review of the nonlocal heat-flow models LMV and AWBS, discuss their limitations, propose an alternative model, and resolve the numerical problems in dealing with their implementation. Also, in order to adequately test the new nonlocal model, comparisons are made with the one-dimensional (1-D) version of the FP code SPARK,<sup>2</sup> which has been improved and changed to Lagrangian form.

### Nonlocal Heat-Flow Formulas

The most general form of the convolution formula in 1-D is given by

$$q(x) = \beta^{-1} \int_{-\infty}^{\infty} dx' q_{SH}(x') G(x, x'), \quad (2)$$

where  $G$  is the delocalization kernel and  $\beta = \int G dx'$  is a normalization factor.

### A. The LMV and AWBS Models

Comparing Eq. (2) to Eq. (1) shows that for the LMV model

$$G_{\text{LMV}}(x, x') = \frac{\exp[-\theta(x, x')]}{2a\lambda_e(x')}, \quad (3)$$

where  $a = 32$ . This value of  $a$  was chosen by Luciani, Mora, and Virmont<sup>5</sup> by comparison with FP code simulations.

The AWBS formula can be derived directly from the following simplified form of the FP equation,<sup>6</sup>

$$-\frac{\partial}{\partial x} \left[ \frac{\lambda_{90}}{3} \frac{\partial(f_{\text{MB}} + \delta f)}{\partial x} \right] = \frac{m\nu^2}{\lambda_\varepsilon} \frac{\partial \delta f}{\partial \varepsilon}, \quad (4)$$

where  $f_{\text{MB}}$  is the Maxwell-Boltzmann (MB) distribution function,  $\delta f$  is a correction to  $f_{\text{MB}}$ ,  $\lambda_{90} = (m\nu^2)^2/4\pi n e^4 (Z \ln \Lambda_{ei} + \ln \Lambda_{ee})$  is the  $90^\circ$  electron angular-scattering mean-free path,  $\lambda_\varepsilon = (m\nu^2)^2/4\pi n e^4 \ln \Lambda_{ee}$  is the energy-loss mean-free path, and  $\varepsilon = m\nu^2/2 - e\phi$  is the total energy variable. The terms on the LHS and RHS of Eq. (4) represent contributions due to spatial diffusion and energy loss, respectively. By further assuming that  $\varepsilon \gg -e\phi$ , Eq. (4) can be solved analytically to yield the following nonlocal heat-flow formula:<sup>6</sup>

$$\{j, q_{\text{AWBS}}\} = -\frac{(\lambda_{90}/\lambda_\varepsilon)^{1/2}}{4\pi(3m)^{1/2}} \int_{-\infty}^{\infty} dx' n T^{-1/2} \{1, T\} \left[ \frac{\partial T}{\partial x'} \{I, K\} - \frac{e \partial \phi_{\text{NL}}}{\partial x'} \{J, L\} \right]. \quad (5)$$

Here,  $j$  is the electric current (which is zero for 1-D thermal transport), and  $\phi_{\text{NL}}$  is the nonlocal contribution to the electric potential. The propagators  $I$ ,  $J$ ,  $K$ , and  $L$  have been defined by Albritton *et al.*<sup>6</sup> in terms of integral functions. Although the contribution of the electric field to the heat flow has been introduced in an explicit form, it is possible to recast Eq. (5) into the general form of Eq. (2).<sup>9,11,12</sup> In fact, like the LMV formula, Eq. (5) reduces to the classical expression  $q_{\text{SH}}$  in the collisional limit.

The validity of both the LMV and the AWBS model relies on the following important assumptions: (1) The kernel  $G$  varies on the slow hydrodynamic time scale, rather than the fast time scale of the evolution of the electron-distribution function. This allows the incorporation of the nonlocal model in fluid codes, where the numerical integration time is governed mainly by the hydrodynamics of the plasma. (2) A small group of fast unthermalized electrons (with energies of about  $7T$ ) are responsible for carrying the bulk of the heat flow, as compared to the thermalized MB distribution of background electrons. Such an assumption permits a simplification of the original FP equation, making it easier to solve analytically. (3) The plasma is of infinite extent. The main implication of this last assumption is that special care is needed in dealing with the spatial boundaries.

The reliability of nonlocal models is normally assessed by comparing their predictions to FP simulations. These comparisons have demonstrated varying degrees of success for the LMV model (and variations of it), and relatively more success for the AWBS model.<sup>5-10,12,13</sup> Unfortunately, because of computational limitations in the FP simulations, the comparisons have usually been restricted to motionless fluids, high initial plasma temperatures (~100 eV), and short laser pulses (~100 ps).

A simpler, but potentially more useful, test consists of calculating the thermal decay of a temperature perturbation in a uniform plasma.<sup>14</sup> The energy equation (neglecting hydrodynamics)

$$\frac{3}{2}n \frac{\partial T}{\partial t} + \nabla \cdot \mathbf{q} = 0, \tag{6}$$

is solved with the initial condition  $T(x, t = 0) = T_0 + \delta T(0)\exp(ikx)$  to yield  $\delta T(t) \propto \exp(-\gamma t)$ . Assuming classical transport, the thermal decay rate is given by  $\gamma_{SH} = 2k^2\kappa_{SH}/3n$ . We can then apply the same perturbation to the FP equation, numerically calculate the asymptotic decay rate defined by  $\gamma_{FP} = 2k^2\kappa_{FP}/3n$ , and obtain  $\kappa_{FP}/\kappa_{SH}$  for a given wave number  $k$ . This test has been done using the FP code SPARK, the results of which are plotted in Fig. 48.8 (solid circles) as a function of  $k\lambda_e$ . As expected, in the long-wavelength limit ( $k\lambda_e \rightarrow 0$ )  $\kappa_{FP}/\kappa_{SH} \rightarrow 1$ . As the perturbation wavelength becomes much shorter than  $\lambda_e$ , a significant reduction in the effective  $\kappa$  is observed. This effect is not new and has been previously discussed in the context of ion waves,<sup>4</sup> thermal smoothing,<sup>2</sup> and laser thermal filamentation.<sup>15</sup> The flux inhibition occurs as a result of nonlocal transport of heat-carrying electrons (with energies of about  $7T$ ) across several wavelengths.

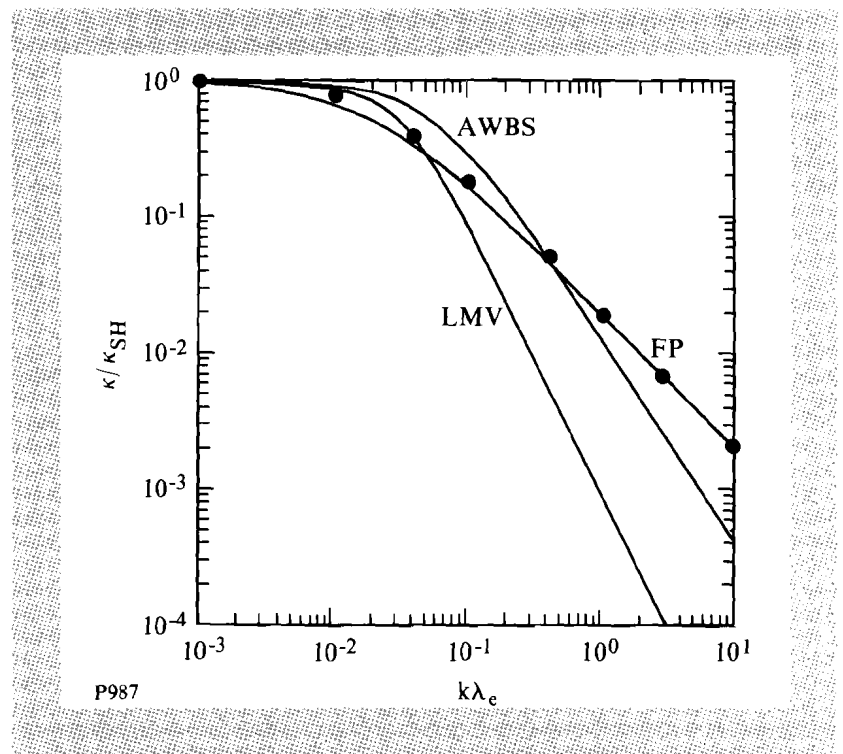


Fig. 48.8 Heat-conductivity spectrum. Ratio of effective conductivity  $\kappa$  to Spitzer-Härm conductivity  $\kappa_{SH}$  as a function of  $k\lambda_e$ , where  $k$  is the perturbation wave number and  $\lambda_e$  is the electron delocalization length. Filled circles correspond to SPARK simulations.

It is straightforward to apply the thermal decay test to the nonlocal heat-flow models discussed in this article. Substituting the LMV formula into Eq. (6) and taking the Fourier transform we obtain<sup>14</sup>

$$\frac{\kappa_{\text{LMV}}}{\kappa_{\text{SH}}} = \frac{1}{1 + (ak\lambda_e)^2}. \quad (7)$$

The ratio  $\kappa_{\text{LMV}}/\kappa_{\text{SH}}$  is plotted in Fig. 48.8 as a function of  $k\lambda_e$ . Repeating the same procedure with the AWBS formula requires numerical integration of the propagators.<sup>16</sup> The result is also plotted in Fig. 48.8.

By comparing the curves in Fig. 48.8, it is clear that neither the LMV nor the AWBS models agree with the FP results, with the former giving the worse agreement. The discrepancy between SPARK simulation results and the AWBS model could be caused by two approximations in the latter: the assumption that  $\partial f/\partial t = 0$ , and the neglect of energy upscattering for the heat-carrying electrons. For large  $k\lambda_e$  both  $\kappa_{\text{LMV}}/\kappa_{\text{SH}}$  and  $\kappa_{\text{AWBS}}/\kappa_{\text{SH}}$  scale as  $1/(k\lambda_e)^2$ , whereas  $\kappa_{\text{FP}}/\kappa_{\text{SH}}$  has a  $1/k\lambda_e$  scaling.<sup>17</sup> Prasad and Kershaw<sup>11</sup> have recently demonstrated that the  $1/(k\lambda_e)^2$  asymptotic dependence of the LMV and AWBS models can lead to unphysical results. They show that, since the decay rate becomes independent of  $k$  for large  $k\lambda_e$  (i.e.,  $\gamma_{\text{LMV}}$  and  $\gamma_{\text{AWBS}} \propto 2\kappa_{\text{SH}}/3n\lambda_e^2$  as  $k\lambda_e \rightarrow \infty$ ), sharp features in temperature will persist indefinitely.

Before proceeding further, it is important to realize that the thermal decay calculation, previously described, is not the only useful test for a nonlocal heat-flow model. It has been shown, for example, that ion motion can play an important role in the energy-transport process. Indeed, ion motion may lead to a phase mismatch between  $\nabla T$  and  $\mathbf{q}$ .<sup>4</sup> Also, inverse-bremsstrahlung (IB) heating can significantly modify the electron-distribution function and hence lead to a modified  $\kappa_{\text{FP}}/\kappa_{\text{SH}}$ .<sup>8</sup> This phenomenon has recently been investigated in the context of laser filamentation, where it was shown that  $[\kappa_{\text{FP}}/\kappa_{\text{SH}}]_{\text{IB}} \approx 1/[1 + (30k\lambda_e)^{4/3}]$ .<sup>15</sup> One may, therefore, conclude that since the *correct* kernel is problem dependent, caution is necessary when applying nonlocal transport models to situations previously untested by the more accurate FP simulations.

## B. An Alternative Nonlocal Heat-Transport Model

The basis of our new model lies in the assumption that the thermal decay spectrum calculated by the FP code SPARK and plotted in Fig. 48.8, provides the most essential information for nonlocal transport. In order to arrive at a useful formula, the spectrum is initially fitted to the FP results, i.e.,  $\kappa_{\text{FP}}/\kappa_{\text{SH}} \approx 1/(1 + ak\lambda_e)$ , by choosing  $a = 50$  (see FP curve in Fig. 48.8). It is now straightforward to take the inverse Fourier transform of this equation and obtain the following kernel in configuration space:

$$G(x, x') = \frac{1}{\pi a \lambda(x')} [-\sin(\theta)\text{si}(\theta) - \cos(\theta)\text{Ci}(\theta)], \quad (8)$$

where  $si$  and  $Ci$  are the sine and cosine integrals, respectively.<sup>18</sup> In order to improve the accuracy of the model, the value of  $\theta$  [given by Eq. (1b)] has been modified by redefining the electron stopping length as  $\lambda_e^* = T^2/4\pi n e^4 (Z^* \phi \ln \Lambda_{ei} \ln \Lambda_{ee})^{1/2}$ , where  $Z^* = \langle Z^2 \rangle \ln \Lambda_{ei} / \langle Z \rangle \ln \Lambda_{ee}$  is the effective charge number ( $\langle \rangle$  denotes an average over the ion species) and  $\phi = (Z^* + 4.2) / (Z^* + 0.24)$ . The inclusion of the factor  $\phi$  is an attempt to correct for the high- $Z$  approximation in the original nonlocal models.

It is of interest to note that for short wavelengths (large  $k\lambda_e$ ) the FP results for  $\kappa/\kappa_{SH}$  (see Fig. 48.8) lie between the (local) SH value  $\kappa/\kappa_{SH} = 1$  and the LMV results, implying that the LMV kernel (3) is “too delocalized.” Therefore, it is not surprising that  $G(x, x')$  lies, in a sense, “between” the SH kernel  $G_{SH}(x, x') = \delta(x - x')$  and  $G_{LMV}(x, x')$ , having some of the properties of each. Both  $G(x, x')$  and  $G_{SH}(x, x')$  diverge for  $x = x'$ , whereas  $G_{LMV}(x, x')$  does not:

$$\lim_{x' \rightarrow x} G(x, x') = \infty, \quad \lim_{x' \rightarrow x} G_{SH}(x, x') = \infty,$$

but

$$\lim_{x' \rightarrow x} G_{LMV}(x, x') = \frac{1}{2a\lambda_e(x)}. \quad (9)$$

On the other hand, the contribution to the heat-flow integral from an infinitesimal region near  $x = x'$  vanishes for  $G(x, x')$  and  $G_{LMV}(x, x')$ , but not for  $G_{SH}(x, x')$ :

$$\lim_{\delta \rightarrow 0} \int_{-\delta}^{\delta} G(x, x') dx' = 0, \quad \lim_{\delta \rightarrow 0} \int_{-\delta}^{\delta} G_{LMV}(x, x') dx' = 0,$$

but

$$\lim_{\delta \rightarrow 0} \int_{-\delta}^{\delta} G_{SH}(x, x') dx' = 1. \quad (10)$$

Thus,  $G(x, x')$  is more sharply peaked at  $x = x'$  than  $G_{LMV}(x, x')$  but less sharply than at  $G_{SH}(x, x')$ , so that it provides an intermediate level of delocalization.

### Numerical Implementation

There are two potential problems with the numerical implementation of nonlocal heat-transport formulas: (a) The inability to smooth out sharp features in temperature profiles, and (b) the possible occurrence of negative values of  $\kappa/\kappa_{SH}$ , which can lead to anti-diffusion instabilities (with the eventual generation of negative temperature distributions). The first problem, discussed in detail in the previous section, results from the  $1/(k\lambda_e)^2$  dependence of the LMS and AWBS models in the limit as  $k\lambda_e \rightarrow \infty$ . One solution is to use a nonlocal model based on FP simulation, which yields a  $1/k\lambda_e$  asymptotic dependence, as described in Part (B) of this article. The second problem is not inherent to the convolution model itself but is a general feature of electron heat transport. FP simulations, under conditions relevant

to ICF, have shown that it is possible for the effective heat flow to be in the direction of  $\nabla T$  (i.e., up the temperature gradient).<sup>1,2</sup>

The occurrence of a negative conductivity, defined by  $\kappa_{FP} = -\mathbf{q}_{FP}/\nabla T < 0$ , need not be a problem provided it is restricted to regions of the plasma where the heat flow is relatively unimportant. Fortunately, extensive FP simulations using SPARK have indicated that this is indeed the case. The effective conductivity tends to become negative mainly in the corona, where the plasma is fairly isothermal, and the magnitude of the heat flow is generally much smaller than in the overdense region. We therefore propose that a simple solution to the problem is to enforce  $\kappa/\kappa_{SH} = 1$ , whenever  $\kappa/\kappa_{SH}$  is initially negative. Thus the anti-diffusion instability is avoided by requiring a positive conductivity. However, when the conductivity is initially positive, the scheme still allows for the possibility of flux inhibition ( $\kappa/\kappa_{SH} < 1$ ) and enhanced heat flux ( $\kappa/\kappa_{SH} > 1$ ).

In practice, the implementation of the numerical scheme involves time-implicit differencing of Eq. (6) in conservative form, i.e.,

$$\begin{aligned} \frac{3}{2}n(T_k^{n+1} - T_k^n) &= \frac{\Delta t}{\Delta x_k}(-q_{k+1/2} + q_{k-1/2})^{n+1} \\ &= \frac{\Delta t}{\Delta x_k} \left[ \frac{\kappa_{k+1/2}^n}{\Delta x_{k+1/2}} (T_{k+1} - T_k)^{n+1} - \frac{\kappa_{k-1/2}^n}{\Delta x_{k-1/2}} (T_k - T_{k-1})^{n+1} \right], \end{aligned} \quad (11)$$

where the effective  $\kappa$  is defined by

$$\kappa_{k+1/2} = -\frac{\Delta x_{k+1/2}}{(T_{k+1} - T_k)\beta_{k+1/2}} \int_{x_{k+1/2}-d}^{x_{k+1/2}+d} dx' G(x_{k+1/2}, x') q_{SH}(x'). \quad (12)$$

Here we have assumed planar geometry, with  $x_k$  and  $x_{k+1/2}$  denoting cell centers and boundaries, respectively. The normalization factor is given by

$$\beta_{k+1/2} = \int_{x_{k+1/2}-d}^{x_{k+1/2}+d} dx' G(x_{k+1/2}, x'). \quad (13)$$

Since the plasma is not of infinite extent, the range of integration is taken from  $x_{k+1/2} - d$  to  $x_{k+1/2} + d$ , where  $d$  is large enough to provide several stopping lengths between  $x_{k+1/2}$  and  $x_{k+1/2} \pm d$ , i.e.,  $\theta(x_{k+1/2}, x_{k+1/2} \pm d) \gg 1$ . By adopting multiple plasma images, the effective  $\kappa$  defined by Eq. (12) also ensures zero heat flux at the plasma boundaries, as is normally required for plasma simulations.

We note from Eq. (12) that  $\kappa$  is not defined when  $T_k = T_{k+1}$  (as would be the case in regions of the simulation yet unperturbed by the heat front). We avoid this problem by evaluating  $q_{k+1/2}$  at the  $n$ th time level (i.e., explicitly) whenever  $|T_{k+1} - T_k| < \eta |T_{k+1} + T_k|$ , where  $\eta$  is a small number (say  $10^{-6}$ ).<sup>13</sup> Another alternative would have been to solve Eq. (11) with  $\kappa$  defined at the

( $n+1$ )th time level. Such an approach, which is the one adopted by Prasad and Kershaw,<sup>11</sup> requires a full-matrix inversion at each time step, involving more computer time than the present method. Our approach also has the added advantage of being more easily appended to an ordinary hydrodynamic code, since it simply redefines  $\kappa$ .<sup>19</sup> In the limit as  $\Delta t \rightarrow 0$  both methods are equivalent.

To test the viability of the nonlocal model we have used SPARK to simulate the heat transport in an idealized plasma, with fixed ions and an initial temperature of 25 eV, irradiated by 351-nm laser at a constant intensity of  $5 \times 10^{14} \text{ W/cm}^2$  over 100 ps. Figure 48.9(a) shows the temperature and density (normalized to the critical density  $n_c$ ) profiles at the end of the simulation. The solid, dashed, and dash-dotted curves refer to the FP, SH, and nonlocal transport calculations, respectively. The corresponding magnitudes of the heat flow are plotted in Fig. 48.9(b).

A comparison of the FP and SH curves in Fig. 48.9 serves to illustrate the typical features of nonlocal transport: flux inhibition of the main heat front, preheat in the cold overdense plasma, and heat flux directed up the temperature gradient in the corona. The simulation using the new nonlocal heat-transport formula is shown to be in reasonable agreement with the FP results. Despite the potential destabilizing influence of the anti-diffusion instability, we were also able to perform the nonlocal formula calculation allowing for  $\kappa/\kappa_{SH} < 0$ . The main effect of forcing  $\kappa/\kappa_{SH} > 0$  is to flatten the

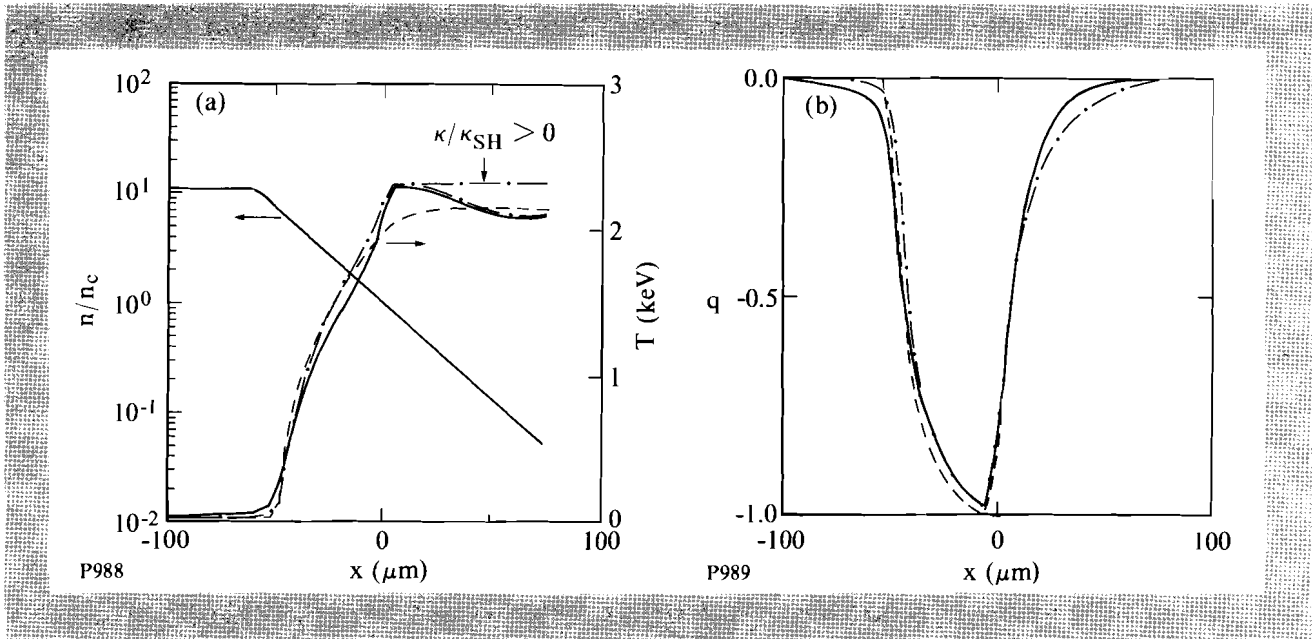


Fig. 48.9  
 Idealized plasma simulation. Plots of (a) electron number density (normalized to the critical density) and temperature in keV, and (b) heat flow (in arbitrary units) as functions of space. Solid, dashed, and dash-dotted curves correspond to FP, SH, and nonlocal heat-flow formula simulations, respectively.

coronal temperature profile (see curve  $\kappa/\kappa_{\text{SH}} > 0$  in Fig. 48.9). However, the influence on the overdense temperature distribution is negligible.

### Simulation of a Laser-Driven Implosion

Until now, the accuracy of nonlocal models has been tested under idealized plasma conditions, such as those described in the previous section. It is, therefore, important to test them under more realistic conditions pertaining to laser-driven ICF. These normally involve variations of several orders of magnitude in temperature and density, hydrodynamic effects, and spherical convergence. In order to simulate these conditions the 1-D version of the FP code SPARK has been improved and converted to spherical geometry in a Lagrangian scheme.

Here, we model the implosion of a fully ionized 10- $\mu\text{m}$ -CH shell of 150- $\mu\text{m}$  radius, irradiated by a 351-nm laser with a 600-ps-FWHM Gaussian pulse of peak intensity  $5 \times 10^{14} \text{ W/cm}^2$ . The target is initially at a temperature of 1 eV and is divided into 40 uniformly distributed 0.25- $\mu\text{m}$  spatial cells. A nonuniform velocity mesh is used for the electron-distribution function, such that  $v_j$  is the velocity of the  $j$ th cell center (where  $j = 1, \dots, 50$ ),  $\Delta v_{j+1}/\Delta v_j = 1.08$  is the ratio of the widths of two adjacent velocity cells, and  $(1/2)mv_{50}^2 = 18.6 \text{ keV}$  is the maximum energy group.

Figure 48.10 shows plots of electron number density (normalized to the critical density  $n_c$ ) and temperature in electron volts. Early in the simulation (at  $-500 \text{ ps}$  with respect to the peak of the laser pulse) the plasma is still relatively cold and collisional, so that there is little difference between SH (dashed curves) and FP (solid curves) results. The times 200 ps and 400 ps correspond to before and after the shock reaches the center of the target, respectively. Note that there is a significant difference between SH and FP calculations, both in terms of peak density, and ablation-surface temperature. As a result of  $\sim 2 \text{ keV}$  coronal temperatures, electrons from that region are able to stream relatively unimpeded through the overdense plasma to deposit their energy at the ablation surface. This preheating phenomenon has the effect of degrading the compression efficiency, with a subsequent lowering of the target's peak density. This type of effect has also been reported by Mima *et al.* for CH targets illuminated by 531-nm laser light.<sup>20</sup>

Although preheat is seen to cause a significant difference in the peak density, other observables, such as the total fractional absorption of light and implosion time, which are more sensitive to the penetration of the main heat front, remain relatively unaffected by the FP treatment. For these, closer agreement between FP and SH calculations can be obtained with the use of a simple flux limiter on the latter.

The previous simulation has been repeated with the use of the nonlocal model developed in this article. Results are plotted in Fig. 48.9 as dash-dotted curves. Comparison with the FP results shows the nonlocal model to be in reasonable agreement with the former, apart from a slight underestimation of preheat.

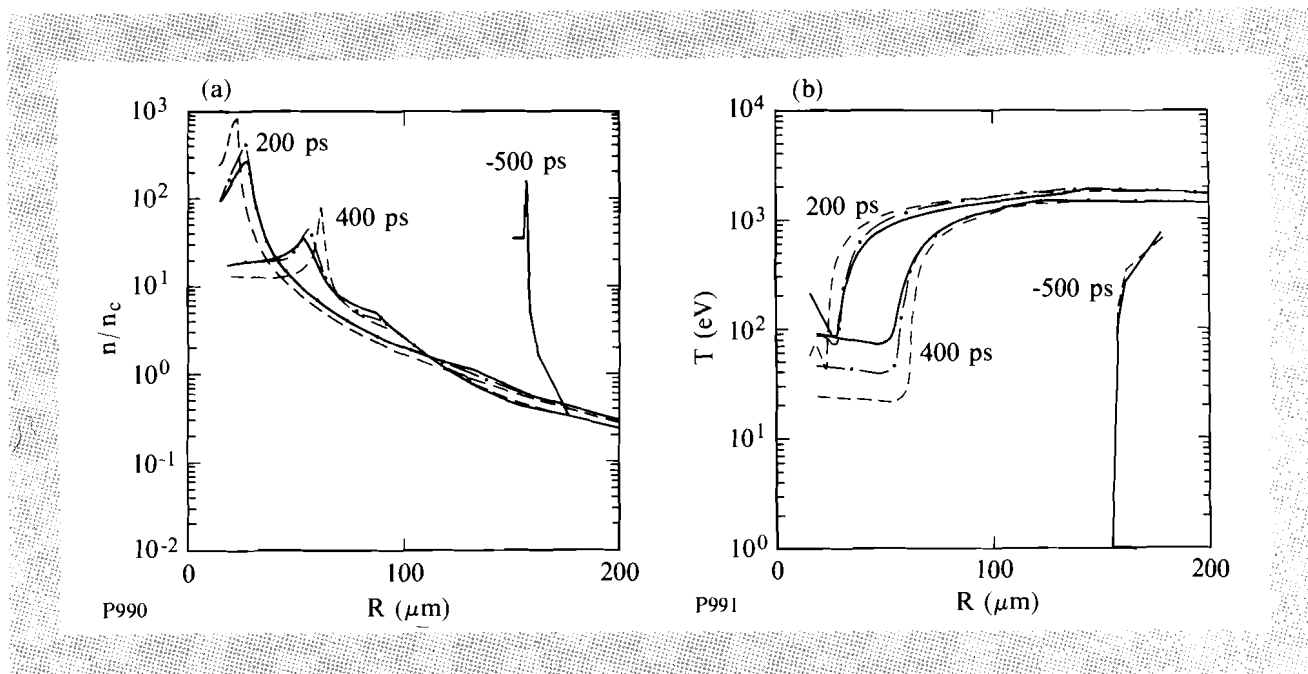


Fig. 48.10

Simulation of a laser-driven implosion. Plots of (a) electron number density and (b) temperature, as functions of space. Curves are identified as in Fig. 48.9.

It is important to point out at this stage that the accuracy of our nonlocal transport model is only as good as the accuracy of the FP model itself. Although the hydrodynamic and electron transport treatment in SPARK has been improved, the code still assumes full ionization (even at the initial temperature of 1 eV), an ideal equation of state, and no radiation effects. In particular, the inclusion of energy loss because of collisional ionization in the cold target could severely reduce the preheat caused by the long mean-free-path electrons. Radiation preheat is relatively weak in CH, but for higher- $Z$  targets this type of preheat may dominate.

### Summary and Conclusions

With the help of a simple test involving the decay of linear thermal waves, we have been able to assess the accuracy of two types of nonlocal formulas (initially developed by Luciani *et al.*<sup>5</sup> and Albritton *et al.*<sup>6</sup>) by comparing their predictions with those based on FP simulations. The resulting spectrum of  $\kappa/\kappa_{\text{SH}}$  as a function of  $k\lambda_e$  indicates a potential problem that may arise in the numerical implementation of certain nonlocal models. The problem is associated with the functional behavior of  $\kappa/\kappa_{\text{SH}}$  for large  $k\lambda_e$ . If  $\kappa/\kappa_{\text{SH}} \propto 1/(k\lambda_e)^2$ , as is the case for the LMV and AWBS models, the thermal decay rate becomes independent of  $k$  and sharp features in temperature profiles do not decay in any finite time. The spectrum of  $\kappa_{\text{FP}}/\kappa_{\text{SH}}$  as a function of  $k\lambda_e$  has also provided the basis for the derivation of a new nonlocal model that avoids this thermal decay problem.

Another difficulty associated with the practical implementation of nonlocal models has been their prediction of heat flux directed along  $\nabla T$ , with the subsequent occurrence of anti-diffusion instabilities. A straightforward solution to this problem is to enforce SH heat flow whenever the situation  $\mathbf{q} \cdot \nabla T > 0$  arises. The justification for this procedure comes from comparisons with full FP simulations under idealized plasma conditions. The model also compares reasonably well with a SPARK FP simulation of a laser-driven implosion of a fully ionized CH shell.

Our motivation for nonlocal heat-transport modeling of ICF targets has come from the prediction of significant preheat (resulting from coronal electrons) in the ablation region with a subsequent reduction in compression efficiency. However, it must be stressed that both the FP code and the convolution formula developed in this article have omitted ionization and radiation physics. The future inclusion of these phenomena could substantially mitigate the preheating effects presently discussed.

#### ACKNOWLEDGMENT

We would like to acknowledge many helpful discussions with J. R. Albritton, W. E. Alley, M. K. Prasad, R. A. Sacks, S. V. Weber, and E. A. Williams. While this manuscript was in progress we were made aware of similar work by M. K. Prasad and D. S. Kershaw. This work was supported by the U.S. Department of Energy Office of Inertial Confinement Fusion under agreement No. DE-FC03-85DP40200 and by the Laser Fusion Feasibility Project at the Laboratory for Laser Energetics, which is sponsored by the New York State Energy Research and Development Authority and the University of Rochester.

#### REFERENCES

1. A. R. Bell, R. G. Evans, and D. J. Nicholas, *Phys. Rev. Lett.* **46**, 243 (1981); J. R. Albritton, *Phys. Rev. Lett.* **50**, 2078 (1983); J. P. Matte, T. W. Johnston, J. Delettrez, and R. L. McCrory, *Phys. Rev. Lett.* **53**, 1461 (1984); A. R. Bell, *Phys. Fluids* **28**, 2007 (1985); T. H. Kho and M. G. Haines, *Phys. Fluids* **29**, 2665 (1986).
2. E. M. Epperlein, G. J. Rickard, and A. R. Bell, *Phys. Rev. Lett.* **61**, 2453 (1988); E. M. Epperlein, G. J. Rickard, and A. R. Bell, *Comput. Phys. Commun.* **52**, 7 (1988).
3. R. C. Malone, R. L. McCrory, and R. L. Morse, *Phys. Rev. Lett.* **34**, 721 (1975).
4. A. R. Bell, *Phys. Fluids* **26**, 279 (1983).
5. J. F. Luciani, P. Mora, and J. Virmont, *Phys. Rev. Lett.* **51**, 1664 (1983).
6. J. R. Albritton *et al.*, *Phys. Rev. Lett.* **57**, 1887 (1986).
7. J. F. Luciani, P. Mora, and R. Pellat, *Phys. Fluids* **28**, 835 (1985); J. F. Luciani, P. Mora, and A. Bendib, *Phys. Rev. Lett.* **55**, 2421 (1985); E. L. Lindman and K. Swartz, *Phys. Fluids* **29**, 2657 (1986); A. Bendib, J. F. Luciani, and J. P. Matte, *Phys. Fluids* **31**, 711 (1988).
8. J. F. Luciani and P. Mora, *Phys. Lett. A* **116**, 237 (1986).
9. F. Minotti and C. Ferro Fontán, *Phys. Fluids B* **2**, 1725 (1990).

10. J. R. Sanmartin, J. Ramirez, and R. Fernandez Feria, *Phys. Fluids B* **2**, 2519 (1990); G. Murtaza, A. Mirza, and M. S. Qaisar, *Phys. Lett. A* **144**, 164 (1990); G. Murtaza, A. Mirza, and M. S. Qaisar, *Plasma Phys. Control. Fusion* **33**, 215 (1991).
11. M. K. Prasad and D. S. Kershaw, *Phys. Fluids B* **1**, 2430 (1989).
12. P. A. Holstein and A. Decoster, *J. Appl. Phys.* **62**, 3592 (1987).
13. P. A. Holstein, J. Delettrez, S. Skupsky, and J. P. Matte, *J. Appl. Phys.* **60**, 2296 (1986).
14. E. M. Epperlein, "Electron Kinetics in Laser-Driven Inertial Confinement Fusion," to be published in *Proceedings of the Topical Conference on Research Trends in Nonlinear and Relativistic Effects in Plasmas*, San Diego, CA, February 1990; LLE Review **42**, 57 (1990).
15. E. M. Epperlein, *Phys. Rev. Lett.* **65**, 2145 (1990).
16. Numerical integration has been kindly provided by E. A. Williams (private communication).
17. J. R. Albritton and E. A. Williams (private communication).
18. W. Gautschi and W. F. Cahill, *Handbook of Mathematical Functions*, edited by M. Abramowitz and I. A. Stegun (Dover Publications, Inc., New York, 1970), p. 231.
19. This current version of the nonlocal heat-flow formula has been successfully added to the *LILAC* hydrodynamic code at the LLE, University of Rochester.
20. K. Mima *et al.*, *Laser Part. Beams* **7**, 487 (1989).

## Section 2

# ADVANCED TECHNOLOGY DEVELOPMENTS

### 2.A Explosion Fraction Measurements on Water-Cooled Xenon Flashlamps

Large-bore, xenon-filled flashlamps have been the main pump source for all Nd:glass fusion drivers. The graybody emission of these lamps at high loadings approximates a 10,000 to 14,000° K blackbody. This is as measured in the wavelength regions of significant Nd<sup>3+</sup> absorption and occurs over a time comparable to the fluorescence lifetime of the Nd<sup>3+</sup> ion (~300 ms). The lamps are made of fused quartz tubing with 1.5- to 2.5-mm-thick walls and have bore diameters in the range of 1.5 to >2.0 cm. Typical arc lengths, measured from electrode to electrode, range from 25 cm to >200 cm. Xenon gas, used for its high electrical-to-optical conversion efficiency, fills the lamp to 300 Torr. Seals at either end connect the quartz tube to electrical connectors. Typical designs are shown in Fig. 48.11.

Because of the high energies involved per lamp (>10 kJ) and the high peak powers (>20 MW), simple L-C circuits are used to drive these lamps. A switch is included to prevent prefiring of the lamps. Circuit resistance is carefully controlled to limit losses. A small (< 500-mΩ) resistive loss may be left to limit peak currents in case of a fault at the lamps. An OMEGA rod-amplifier drive circuit is shown schematically in Fig. 48.12. Figure 48.13 shows the circuit currently used in a prototype disk amplifier at LLE. The disk-amplifier circuit has the additional capability of ionizing the lamps several hundred microseconds prior to the main discharge.

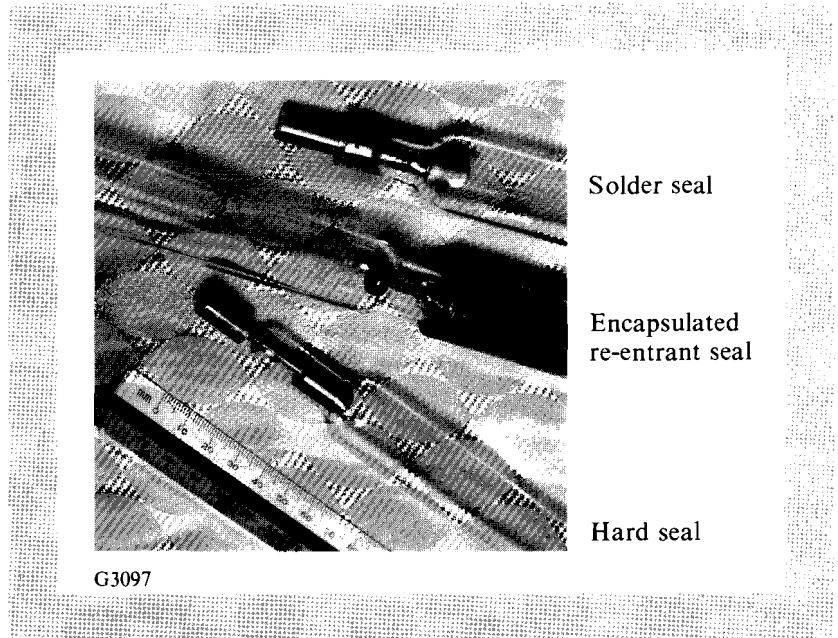


Fig. 48.11  
 Three flashlamp designs. The top lamp is a water-cooled, solder-seal design. The middle lamp is an encapsulated re-entrant seal design. Part of the lamp seal is covered by the metal end tube. The bottom lamp is a water-cooled, hard-seal lamp used in the disk amplifier.

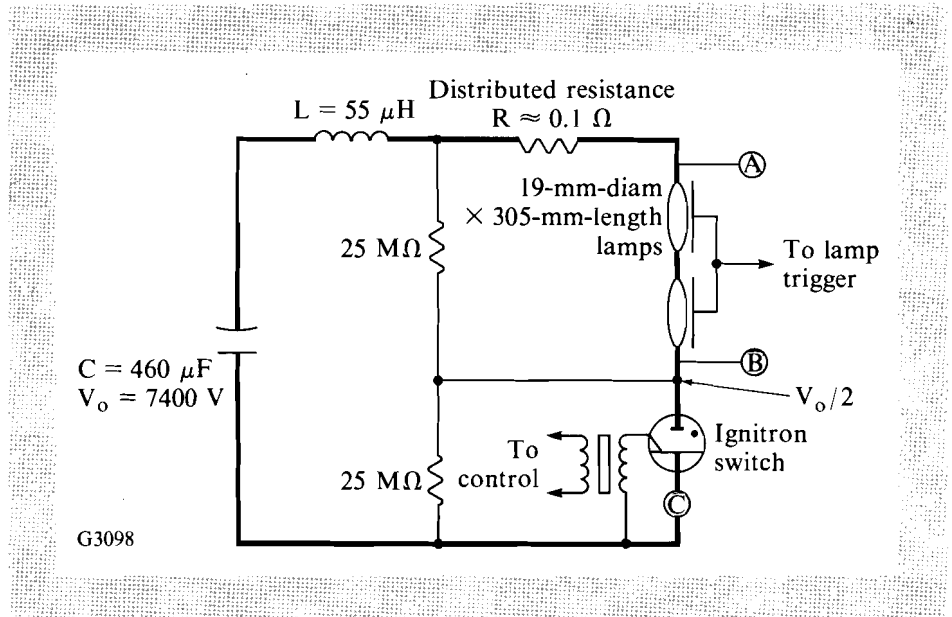


Fig. 48.12  
 Drive circuit used for OMEGA rod amplifiers. Differential voltage measurement was made at point A and point B. Current was measured at point C. Charging circuitry is not shown.

These large flashlamps, when operated in air, can experience catastrophic failure.<sup>1</sup> Typically, the lamp envelope fails during the early portion of the shot, breaking up into numerous small (< few millimeters square) pieces that are violently expelled from the arc region. The cause of these failures is still uncertain, but several hypotheses have been advanced: (a) small cracks in regions of the envelope placed under severe tensile stress during the shot, (b) pre-existing regions of stress in the lamps, (c) excessive Lorentz forces from neighboring lamps, and (d) power-conditioning failures that electrically overload the lamps. Catastrophic failures can be particularly costly in disk-geometry amplifiers where large, polished surfaces of laser glass face the flashlamps. Blast windows are used in disk amplifiers to limit damage from such an event.

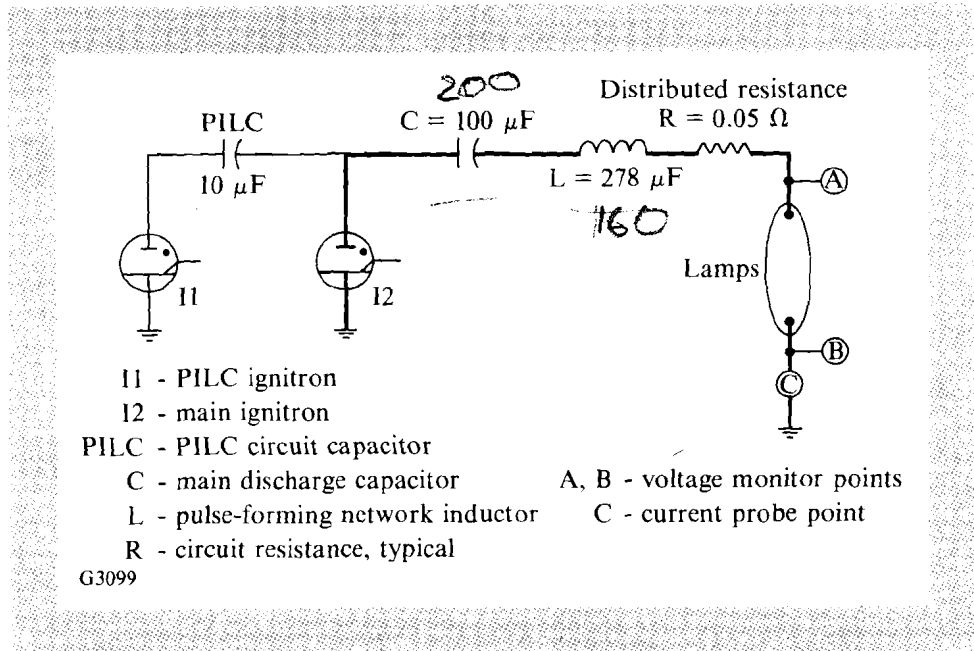


Fig. 48.13  
 Drive circuit for the prototype disk amplifier.

A measure of the average number of shots until failure of an air-cooled flashlamp was developed a number of years ago<sup>2</sup> based on the so-called explosion fraction at which the lamp operates. The number of shots  $N$  expected before failure is given by

$$n \sim \left( \frac{E_o}{E_x} \right)^{-8.5}$$

where  $E_o$  is the total energy in joules delivered to the lamp, and  $E_x$  is the explosion energy of the lamp in joules calculated from the empirically determined expression  $E_x = 2 \times 10^4 ld(LC)^{1/4}$ , where  $l$  and  $d$  are the arc length and bore in cm, and  $L$  and  $C$  are the inductance in henrys and

capacitance in farads of the driving circuit, respectively. The ratio  $E_o/E_x$  is denoted  $f_x$  and is known as the explosion fraction. A typical large, air-cooled lamp might operate at 15%–20% explosion fraction.

Extensive quality-control programs have been developed<sup>3</sup> that minimize the occurrence of catastrophic failure in air-cooled lamps operated at 15%–20% of explosion fraction. Important steps in these programs include infant mortality testing at elevated explosion fractions ( $>30\% f_x$ ) for a limited number of shots, microscopic inspection of the quartz walls of each lamp for cracks,<sup>4</sup> and inspection in a polarimeter for regions of wall stress.<sup>5</sup>

The OMEGA system contains 680 1.9-cm bore by 30-cm arc-length lamps. The OMEGA lamps are water cooled by operating the lamps inside 25-mm-ID Pyrex™ water jackets. The original OMEGA design called for operation of the lamps at an explosion fraction of 30% as defined for air-cooled lamps. Fewer than six catastrophic failures have been observed over the 23,000+ shot lifetime of the system despite the relatively high operational explosion fraction. Even these few catastrophic failures were relatively benign, resulting in large fragments that generally remained in the original lamp vicinity. The more typical fault mode is a failure to trigger, which is often caused by the lamp filling with water. Incoming lamp inspection for OMEGA has been limited to dimensional checks and tesla-coil tests for lamp breakdown.

The large amount of pump energy required for the disk amplifiers in a laboratory microfusion facility (LMF) has led to an interest in large-bore lamps operated at relatively high explosion fractions (30%–40%). This is to minimize costs. Water cooling offers the potential for substantially reducing the possibility of catastrophic failure at high explosion fractions. A cooperative effort between groups<sup>6</sup> at LLE and Lawrence Livermore National Laboratory is attempting to understand OMEGA's outstanding experience with large-bore, water-cooled lamps.

The first step in understanding OMEGA's success was to determine the actual explosion fraction at which the OMEGA lamps are operated. This required precision measurements of the instantaneous voltage across the lamps and the instantaneous current through them. A joint LLE/LLNL team performed these measurements; the results are described in this article.

Two flashlamp drive circuits were tested. The first circuit was a spare 90-mm-rod amplifier module for the OMEGA system. The equipment was in every way identical to actual OMEGA hardware. The second circuit was a disk amplifier test circuit driving a single, isolated "brick" of five flashlamps, connected in series, and located in a large enclosure. Voltage measurements were made as close as possible to the lamps to reduce the inductive and resistive effects of the interconnecting wire. About 1.5 m of #6-gauge wire was used to connect the probe to the lamp-end electrodes. Differential voltage measurements were performed across the lamps on both systems to eliminate ground-referencing problems.

The measurements were made using LLNL-supplied current transformers and voltage probes. The voltage probes (Tektronix P6015) were calibrated just prior to the experiment at the LLNL calibration facilities to an accuracy of  $\pm 2\%$ . The current probe (Pearson, Inc.) was calibrated by the manufacturer, also to an accuracy of  $\pm 2\%$ . Data was recorded on two Tektronix 2440 digitizing oscilloscopes, which were calibrated in 1990 to a vertical (voltage) accuracy of  $\pm 2\%$ . The time base on the oscilloscopes is crystal controlled and has a manufacturer-stated accuracy of 0.00015%. The resulting overall accuracy of these measurements is approximately 3% for current or voltage and 4% for power or energy. The resulting possible error for the explosion fraction is 7% of the measured fraction; the additional error is caused by inaccuracies in measurements of the circuit parameters and lamp dimensions. The accuracy of the probes and current transformers was consistency-checked with LLE equipment.

The lamps in the OMEGA rod amplifier are triggered into conduction by a high-voltage, low-power trigger pulse applied to a backplane adjacent to the lamp. The ignitron switch is triggered simultaneously with the lamp. The lamp current rises as its impedance drops. Eventually, all of the energy stored in the capacitor is delivered to the lamps.

The disk amplifier circuit includes a pulsed lamp-preionization circuit (PILC).<sup>7</sup> The PILC pulse serves to ionize most of the gas volume in the flashlamp prior to the main discharge initiation. Ignitron "I1" is fired 250  $\mu$ s before the main ignitron "I2," discharging the PILC storage capacitor into the lamps. The combination of this capacitor and the inductor "rings up" the voltage on the cable capacitance high enough to provide initial lamp breakdown. In both the OMEGA rod- and disk-amplifier circuits the voltage was monitored at points A and B (see Figs. 48.12 and 48.13), recording the signals in separate oscilloscope channels. Lamp current was monitored at point C.

Sample voltage and current waveforms versus time are shown in Figs. 48.14 and 48.15 for the rod and disk amplifiers, respectively. Instantaneous power in the lamps is shown in Figs. 48.16 and 48.17 for the same charging voltage. The time integral of the instantaneous power over the entire pulse was calculated using a commercial spreadsheet program. In Figs. 48.18 and 48.19 the explosion fraction is plotted versus charging voltage. Typically, OMEGA rod amplifiers operate at 7.4-kV charging voltage ( $V_0$ ), which corresponds to a delivered explosion fraction of 34%. The corresponding explosion fraction for the disk amplifier's 13.5-kV charge voltage is 25%.

The current waveforms displayed in Figs. 48.14 and 48.15 are the classical near critically damped waveforms. This was the design criterion for the circuit. The voltage waveforms for both the rod and the disks display several features: At point A in the plots there is a brief spike that is the lamp trigger. Then the voltage drops rapidly as the arc expands to fill the bore of the lamp at point B. The modulation observed on the traces at point C is hypothesized to be caused by acoustic effects inside the lamp. Efforts are underway to

correlate this signature with accelerometer measurements. Finally, the voltage decays as all of the bank energy is dissipated.

In conclusion, these measurements indicate that the water-cooled flashlamps used in the OMEGA laser system have been routinely operating at a delivered explosion fraction of 34% without catastrophic failure. Furthermore, this has been accomplished without the use of an extensive quality-control program. Thus, large-bore, water-cooled lamps may be an attractive solution for operation at high explosion fractions in LMF-scale laser systems.

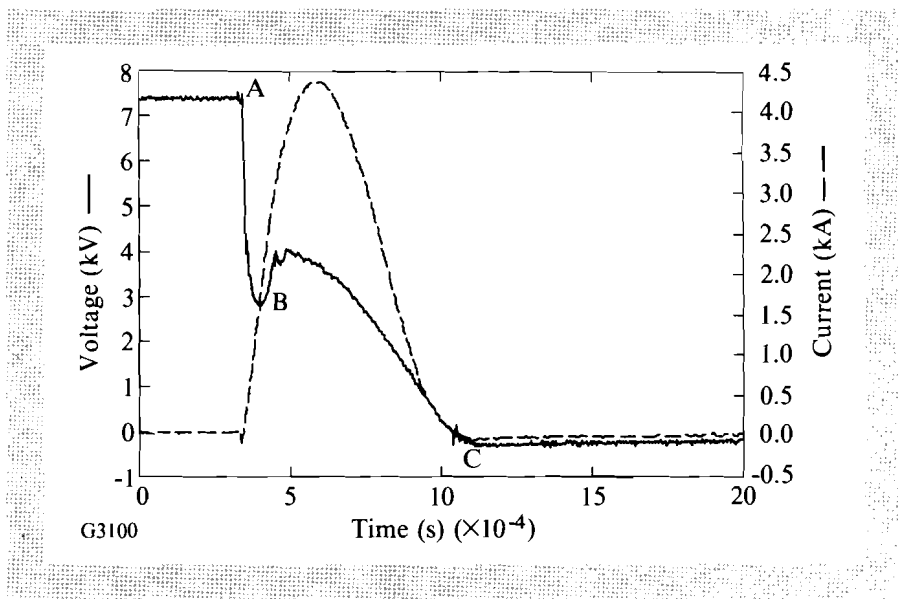


Fig. 48.14 Current and voltage versus time for the 90-mm-rod amplifier at 7.4-kV charging voltage.

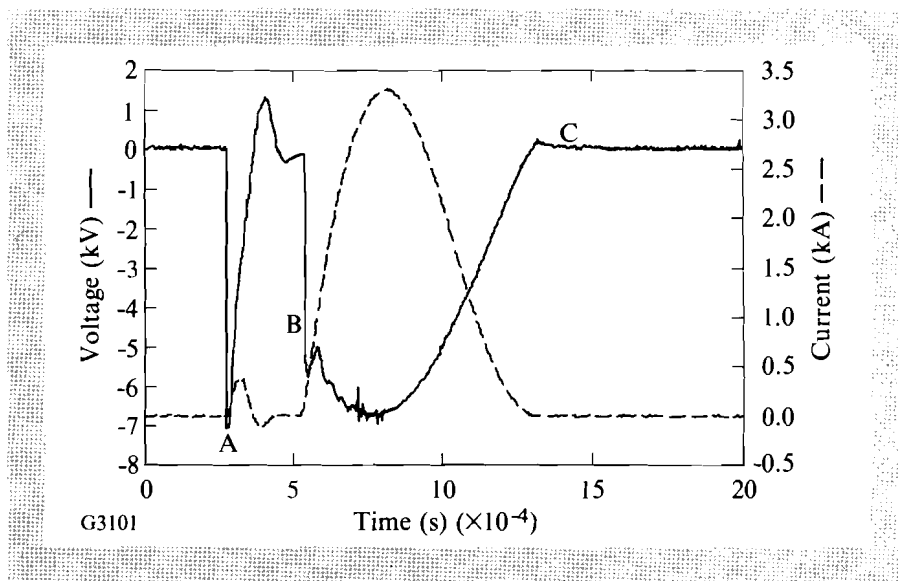


Fig. 48.15 Current and voltage for the prototype disk amplifier at 13.4-kV charging voltage.

Fig. 48.16  
Power versus time for the 90-mm-rod amplifier at 7.4-kV charging voltage.

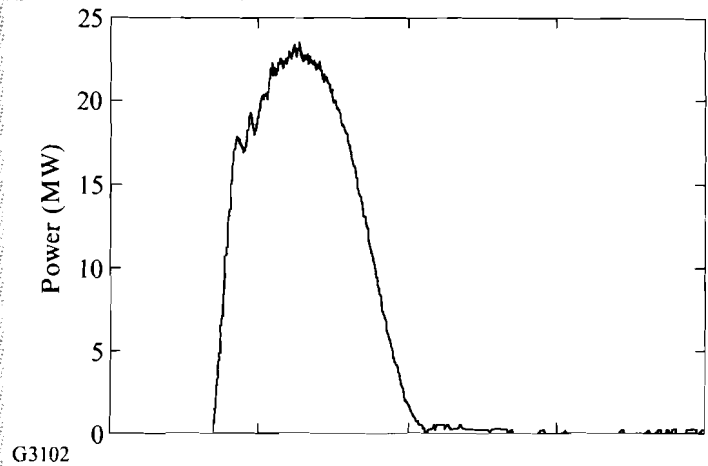


Fig. 48.17  
Power versus time for the prototype disk amplifier at 13.4-kV charging voltage.

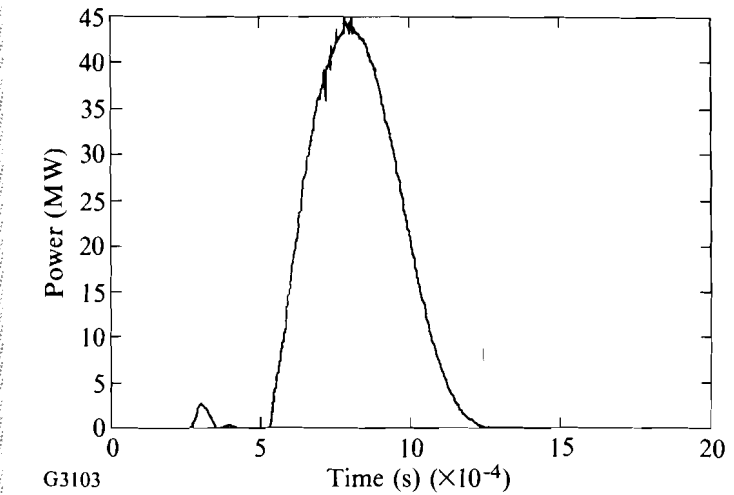
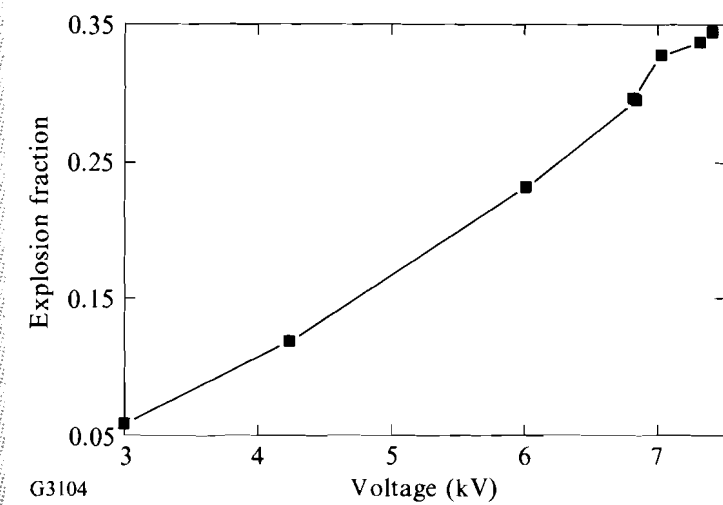


Fig. 48.18  
Explosion fraction for the 90-mm-rod amplifier lamps versus charging voltage.



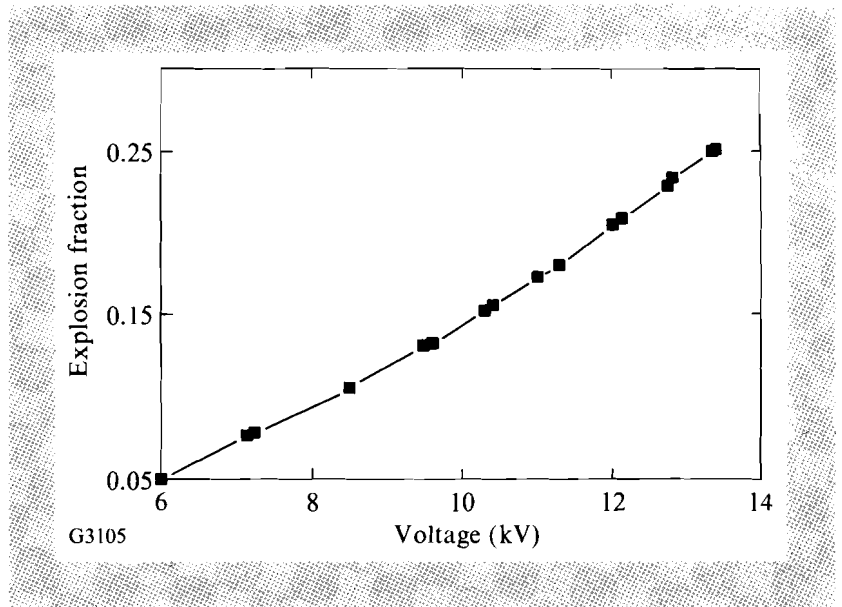


Fig. 48.19  
Explosion fraction for the prototype disk-amplifier lamps versus charging voltage.

#### ACKNOWLEDGMENT

This work was supported by the U.S. Department of Energy Office of Inertial Confinement Fusion under agreement No. DE-FC03-85DP40200 and by the Laser Fusion Feasibility Project at the Laboratory for Laser Energetics, which is sponsored by the New York State Energy Research and Development Authority and the University of Rochester.

#### REFERENCES

1. Laser Program Annual Report 1974, Lawrence Livermore National Laboratory, Livermore, CA, UCRL-50021-74, p. 108 (1975).
2. J. H. Goncz, *Instr. Soc. Am. Trans.* **5**, 28 (1966).
3. Laser Program Annual Report 1975, Lawrence Livermore National Laboratory, Livermore, CA, UCRL-50021-75, pp. 172–177 (1976).
4. Laser Program Annual Report 1975, Lawrence Livermore National Laboratory, Livermore, CA, UCRL-50021-75, p. 176 (1976).
5. K. Yoshido *et al.*, *Rev. Sci. Instrum.* **55**, 1415 (1984).
6. We are indebted to E. A. Campbell, A. C. Erlandson, and D. W. Larson for their efforts on behalf of this collaboration.
7. Laser Program Annual Report 1985, Lawrence Livermore National Laboratory, Livermore, CA, UCRL-50021-85, pp. 7–18 (1986).

## 2.B Perfluorinated Copolymer Coatings for High-Power Laser Applications

Many common crystals for optical parametric processing, i.e., KDP, CDA, etc., are hygroscopic. Preserving their long-term stability and optical quality requires immersion in an index-matching liquid contained in some sort of cell.<sup>1</sup> Several drawbacks derive from this, not the least of which is cost, when up to 1-m beam and cell diameters must be considered for use in fusion-scale laser systems. Technical drawbacks exist as well; losses caused by transverse stimulated Raman scattering in the index-matching liquid, and photodissociation of the liquid by UV light are known to occur. Looking for a simple, cost-effective solution to protect KDP during in-air use, without incurring significant optical losses, led us to explore the benefits of the soluble perfluorinated polymers,<sup>2</sup> Teflon AF-1600 [66-mole-% dioxole (Bis-2, 2-trifluoromethyl-4, 5-difluoro-1, 3-dioxole) 34-mole-% tetrafluoroethylene,  $n^D = 1.31$ ] and Teflon AF-2400 [84-mole-% dioxole (Bis-2, 2-trifluoromethyl-4, 5-difluoro-1, 3-dioxole) 16-mole-% tetrafluoroethylene,  $n^D = 1.29$ ]. The refractive index of 1.29 (of the sodium-D line) is of interest because it is close to the value required for a simple, antireflective, quarter-wave layer on KDP. The refractive index of the copolymers decreases with increasing dioxole content and approaches the ideal refractive index of 1.24 for matching KDP. However, the solubility of the polymers also decreases with increasing dioxole content, precluding the use of the polydioxole or very-high-content dioxole copolymers. With this constraint and the corresponding refractive index mismatch, a quarter-wave layer of AF-1600 on KDP will, at best, reduce the single-surface Fresnel reflection loss of KDP to 0.4% at sodium D.

Whenever these Fresnel losses are acceptable, these perfluorinated coatings offer an attractive, low-cost approach to protecting optics. By now, several solvents exist, not all equally meritorious, in which the copolymers can be dissolved for spin deposition. Spatially uniform films result from an optimized combination of substrate diameter, spinning speed, solvent evaporation rate, solution viscosity, and solvent solubility. Both the tools needed to optimize the process and the required solvents are quite inexpensive when compared to the costs of mounting KDP in conventional cells.

The solvents tested were two pure perfluorinated polyethers,  $C_{10}F_{22}O_2$  (Hostinert 130)<sup>3</sup> and  $C_{22}F_{46}O_6$  (Hostinert 272),<sup>3</sup> and two mixtures of perfluoroalkylamines, (Fluorinert FC-40)<sup>4</sup> and perfluorinated cyclic ethers (Fluorinert FC-75).<sup>4</sup> Before use, the solvents were filtered to remove particulates larger than 1  $\mu\text{m}$ . No further purification was attempted.

In this effort of coating planar KDP surfaces, 2-wt.% solutions of Teflon AF-1600 and Teflon AF-2400 were found optimal. Solutions with up to 10-wt.% concentration of Teflon AF-1600 were prepared, indicating that

highly viscous solutions can be made if desired. Films were cast on clean substrates under clean-room conditions. For curing and solvent removal, samples were kept at 100°C for 12 h. For KDP, much higher curing temperatures are not advisable.

Film thickness was derived from spectrophotometric scans covering the 300- to 1080-nm range. A typical scan in Fig. 48.20 plots differential absorbances (an uncoated reference sample of identical thickness was placed in the spectrophotometer reference arm) against wavelength. The transmission maxima near 350 nm and 1050 nm resulting from the single, coated surface are evident in Fig. 48.20. These two wavelengths represent the fundamental and third-harmonic wavelengths of neodymium lasers. The Teflon coating represented by Fig. 48.20 can therefore be used both as an input and exit-face coating on a KDP frequency-tripling unit.<sup>1</sup> The film used for Fig. 48.20 is chosen for illustrative purposes and does not constitute the best achievable, single-layer AR Teflon film on KDP. Here the single-surface reflectivity of KDP is reduced from 4% to 2.5%.

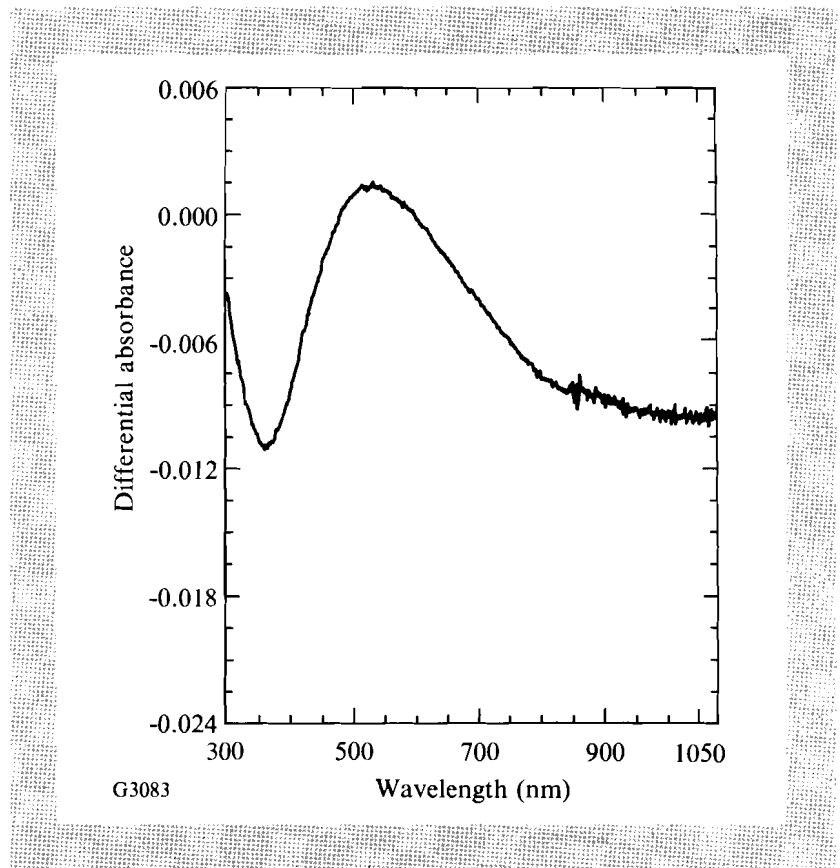


Fig. 48.20

Differential absorption scan of single-surface, Teflon AF-1600-coated KDP. An uncoated, similar-thickness KDP piece was placed in the spectrophotometer reference arm. The film reduced the reflectivity of the uncoated surface by 1.3% at 350 nm.

Optical survival strength is a pivotal criterion in screening materials for high-peak-power laser applications. In general, it is more difficult to meet peak-fluence requirements at shorter wavelengths. We report here 351-nm, 0.8-ns damage-threshold results from similar-thickness, AF-1600 films prepared on various substrates from different solvents. The damage-test substrates were conventionally polished, fused-silica disks and diamond-turned, flat KDP substrates (both 5-cm diam). The 351-nm irradiation spot size was 2 mm in diameter. These measurements yielded the results tabulated in Table 48.I. Damage is impurity driven in all but one solution-derived film. Only one solvent (Hostinert 272) is currently available in adequate purity to assure a film optical survival strength commensurate with multiple  $\text{J}/\text{cm}^2$  applications. All other solvents leave residues in the films that cause sharp drops in damage threshold. This applies to solvents that were passed through 0.5- $\mu\text{m}$ -pore filters. That low-volatility impurities are at fault in this situation can be shown by testing solutions directly. This is done using a prism geometry previously reported.<sup>5</sup> Testing solutions, i.e., samples in which the impurities are highly dilute compared to films, invariably yields thresholds that are about one order-of-magnitude higher than those from films.

For the one solvent without significant impurities, a separate film-damage mechanism can be invoked. Both copolymers are fully saturated and are, as such, expected to exhibit intrinsically high damage thresholds.<sup>5</sup> However, as polymerized, the copolymers contain some acyl fluoride end groups. These end groups are removed in a subsequent process step.<sup>6</sup> The removal success varies somewhat from batch to batch. We tested damage thresholds for the presence of this  $\pi$ -conjugated group by preparing films from specially selected materials that were known to be either high or low in functional end-group density. The results in this case are very clear. Table 48.II shows a threshold improvement by a factor of 3 to 4, going from the Teflon version high in  $\pi$ -conjugated end-group density to the one 17 times lower in end-group density, all dissolved in Hostinert 272. For comparison, the result from a random-batch sample is included in Table 48.II as well. We have not explored which photochemical mechanism causes the *N*-on-1 threshold for this sample to be twice as high as the 1-on-1 threshold.

Table 48.II settles the issue of extrinsic, solvent-induced impurity damage: Hostinert 272 is the only known solvent that permits distinguishing the intrinsic, polymer functional group-derived damage from extrinsic effects. From a laser-systems design standpoint, Table 48.II provides bounds on the fluences at which a given system may safely operate, using coatings derived from standard, commercially available Teflon AF-1600. The single-shot threshold of  $3.26 \text{ J}/\text{cm}^2$  and, even more so, the ramp-up, multiple-shot threshold of  $7 \text{ J}/\text{cm}^2$  rank with the best alternative surface treatment methods.

Finally, we mention that more stringent antireflection requirements for this polymer sealant can be met by reverting to a two-component system. The original implementation of this concept<sup>7</sup> used a different polymer whose

Table 48.I: Laser-damage thresholds (351 nm, 0.8 ns) of Teflon AF-1600 as a function of solvent and substrate. Film thickness is  $\lambda/4$  at 351 nm.

Solvent	Substrate	1-on-1 J/cm <sup>2</sup>	N-on-1 J/cm <sup>2</sup>
FC-75	fused silica	1.89±0.02	2.36±0.61
25%/75% mixture of FC-40/FC-75	fused silica	<0.5	1.29±0.32
Hostinert 130	fused silica	1.90±0.1	1.83±0.60
Hostinert 130	KDP	1.06±0.02	1.50±0.14

G3119

Table 48.II: Effect of functional end-group density on Teflon AF-1600\* laser-damage thresholds (351 nm, 0.8 ns).

	1-on-1 J/cm <sup>2</sup>	N-on-1 J/cm <sup>2</sup>
High density	2.64±0.15	2.19±0.5
Random batch	3.26±0.20	7.1±1.0
Low density	7.75±1.49	8.39±1.51

\*All samples prepared in Hostinert 272

G3120

UV-laser-damage threshold made high-peak-power laser applications questionable. Two approaches are possible: one either seals the crystal surface with polymer first and deposits thereafter a porous sol-gel antireflection layer on top of the polymer, or one reverses the steps and seals the porous structure with the perfluorinated polymer as a barrier on top. We have investigated both approaches. One must note, however, that this layer reversal does not yield the same final transmittance in both cases. In practice, the latter approach is much simpler to implement; there, the Teflon layer is spin deposited on a conventionally prepared, sol-gel AR layer. In the reverse-order process, a challenge arises in the form of poor wettability of the Teflon surface. The key to proper wetting of the Teflon layer is the use of a fluorinated surfactant (FC-171)<sup>4</sup> in the sol-gel solution at about 2% by weight concentration. Several other surfactants have been explored as well,

each one causing pH changes in the sol-gel solution that made control of the sol-gel porosity difficult. The two-component system yields, even without optimized deposition conditions having been established, transmittance through KDP in excess of 99.6% at 351 nm. Equally important, the optical survival strength at this wavelength is not reduced by the increased complexity of the two-component system.

We measured 0.8-ns damage thresholds for this system similar to those listed in Table 48.II:  $6.6 \pm 0.2 \text{ J/cm}^2$  under 1-on-1 conditions, and  $7.8 \pm 1.0 \text{ J/cm}^2$  under *N*-on-1 conditions. These results demonstrate that the perfluorinated copolymer Teflon AF-1600 is a superior medium for sealing hygroscopic frequency-conversion crystals, with the added advantage of providing a damage-resistant antireflection option. The polymer is easily processed and applied and is an inexpensive solution to large-crystal maintenance.

#### ACKNOWLEDGMENT

We thank K. Marshall and B. Puchebner for many helpful suggestions and K. Skerrett for assistance in dip-coating of samples. This work was initiated by funding by NASA (Grant NAG-1-910) and supported by the U.S. Department of Energy Office of Inertial Confinement Fusion under agreement No. DE-FC03-85DP40200 and by the Laser Fusion Feasibility Project at the Laboratory for Laser Energetics, which is sponsored by the New York State Energy Research and Development Authority and the University of Rochester.

#### REFERENCES

1. R. Bossert, S. D. Jacobs, and L. Lund, 14th Annual Symposium on Optical Materials for High Power Lasers, *Nat. Bur. Stand. Spec. Pub. 669* (Government Printing Office, Washington, DC, 1984), p. 118.
2. (a) E. I. DuPont de Nemours and Co. Inc., Specialty Polymers Division, Little Falls Centre, Wilmington, DE; (b) P. R. Resnick, *Polymer Preprints* **31**, 312 (1990).
3. Hoechst Celanese Corporation, Advanced Technology Group, 51 John F. Kennedy Parkway, Short Hills, NJ 07078.
4. 3M Corporation, Industrial Chemical Products Division, St. Paul, MN 55144-1000.
5. M. Guardalben, A. Bevin, K. Marshall, A. Schmid, and F. Kreuzer, in *Laser Induced Damage in Optical Materials: 1988*, *Nat. Bur. Stand. Spec. Pub. 775* (Government Printing Office, Washington, DC, 1989), p. 462.
6. P. G. Bekiarian, M. D. Buckmaster, and R. A. Morgan, U.S. Patent 4,946,902 (1990).
7. I. N. Ross, Rutherford Appleton Laboratory, United Kingdom (private communication).

## 2.C Time-Resolved Study of Surface Disordering of Pb(110)

Melting is one of the most common phase transformations; however, the process is not completely understood as no generally accepted theory exists to provide an understanding of this phenomenon on the atomic level. It is believed that melting is initiated at the surface of a material, at a temperature slightly below the bulk-melting temperature  $T_m$ .<sup>1</sup> This offers an understanding of the lack of parity between supercooling and superheating. A thin, disordered surface layer, formed below  $T_m$ , would act as a nucleus for melting into the bulk at  $T_m$ , thus precluding superheating. Several years ago, the formation of a disordered surface layer on Pb(110) was observed at temperatures below the bulk-melting point.<sup>2</sup> Since then, much work has been undertaken to characterize the thermally induced structural phase transformations that take place at solid surfaces.

Frenken *et al.* provided the first conclusive evidence of surface pre-melting (the formation of a thin, disordered surface layer below  $T_m$ ).<sup>2</sup> Using the ion-shadowing and blocking technique, they showed that the Pb(110) surface exhibits a reversible order-disorder transition below the bulk-melting temperature ( $T_m = 600.7$  K). These ion-shadowing and blocking results were also supported by a reflection high-energy electron diffraction (RHEED) study and infrared emissivity measurements on Pb(110) near  $T_m$ .<sup>2</sup> Further work with ion-shadowing and blocking revealed that the Pb(110) surface begins to disorder in the temperature range of 450–560 K and that the thickness of the disordered layer grows logarithmically in the range  $0.3 \text{ K} \leq \Delta T \leq 40 \text{ K}$ , where  $\Delta T = T_m - T$ .<sup>3</sup> This technique also revealed a change from logarithmic growth of the disordered-layer thickness to a power-law dependence for  $\Delta T < 0.3 \text{ K}$ , which is attributed to the effect of long-range atomic interactions.<sup>3</sup> The pre-melting phenomenon depends on surface packing and, for Pb, is most pronounced for open surfaces such as (110), but is not observed for the close-packed (111) surface.<sup>3</sup>

X-ray photoelectron diffraction (XPD)<sup>4</sup> and low-energy electron diffraction<sup>5</sup> were also used to study surface pre-melting on Pb(110) and provided characteristic temperatures for the onset of surface disorder of  $530 \pm 5$  K and  $543 \pm 3$  K, respectively. Recently, an XPD study on Pb(100) revealed disordering behavior intermediate to that of Pb(110) and Pb(111).<sup>6</sup> X-ray scattering studies have also observed surface pre-melting on Pb(110).<sup>7,8</sup>

Molecular dynamics (MD) simulations dealing with the high-temperature behavior of metals have shown evidence for disordering below the bulk-melting temperature on Al(110),<sup>9</sup> Ni(110),<sup>10</sup> and Au(110).<sup>11</sup> However, these studies did not examine the time evolution of the disordering process. MD studies that deal with time evolution treat the behavior of metal surfaces above the thermodynamic melting point<sup>12,13</sup> as a distinctly different phenomenon than that of surface pre-melting. To our knowledge, currently

available MD studies on metals do not explicitly treat the temporal evolution of surface pre-melting.

There have been many time-resolved studies of laser-induced melting.<sup>14</sup> Picosecond transient reflectance measurements were used to examine the dynamics of the melting of Au and Cu.<sup>15</sup> Crystallization velocities as high as 100 m/s were observed, and it was proposed that the velocity for solidification in metals is limited by the speed of sound. It should be emphasized here that these studies involved bulk melting, that is, the occurrence of a first-order phase transformation. The work described here involves studying the dynamics of the formation of the disordered layer on Pb(110) at temperatures below  $T_m$ . This pre-melting phenomenon is different in that (1) it is a transformation that is continuous over some temperature range, (2) it is known to be reversible at low heating and cooling rates, and (3) it depends on surface structure.

Most of the time-resolved, laser-induced melting work employs classical transition-state theory,<sup>16</sup> which provides satisfactory agreement with experimental results. However, the experimental conditions for the work described here are quite different. First, in the case of surface pre-melting, unlike bulk melting, disordering of the surface occurs below the bulk-melting temperature. Indeed, the nature of the surface order-disorder transition has not been completely characterized. Much evidence suggests that the surface pre-melting phenomenon is a continuous process, as opposed to the abrupt first-order transition that occurs in bulk melting.<sup>2,17</sup> Secondly, the RHEED geometry allows us to probe depths of 10 Å or less. Coupling the surface sensitivity of RHEED with the much larger skin depth of the heating laser pulse (~140 Å in Pb for our experimental conditions) leads to a situation where the probed layers are isothermal to a good approximation. This is to be contrasted with other techniques such as transient reflectance or conductance, which typically probe depths of  $\geq 100$  Å, where temperature gradients are significant. The interesting character of surface pre-melting leads us to study the nature of the disordered-layer growth and reordering processes. Here we report on a time-resolved study of the laser-induced disordering of Pb(110).

The method we use is picosecond RHEED.<sup>18</sup> A schematic diagram of the experimental setup is shown in Fig. 48.21. A picosecond laser pulse is split into two beams. The first beam induces a fast surface-temperature rise on the sample, while the second is incident on the cathode of a photoactivated electron gun, which produces a collimated electron pulse. The energy of the electron pulse in the work reported here was 18.2 keV, and its pulse width was determined by operating the picosecond electron gun as a streak camera,<sup>18</sup> and found to be ~180 ps measured at FWHM. The electron pulse is well synchronized with the heating-laser pulse and is used to generate a RHEED pattern of the surface of the sample. A RHEED pattern from a flat surface consists of a series of streaks or lines, whose separation can be related to the spacing of the atoms at the surface. Typically, each RHEED pattern is obtained by averaging several hundred shots, although single-shot operation

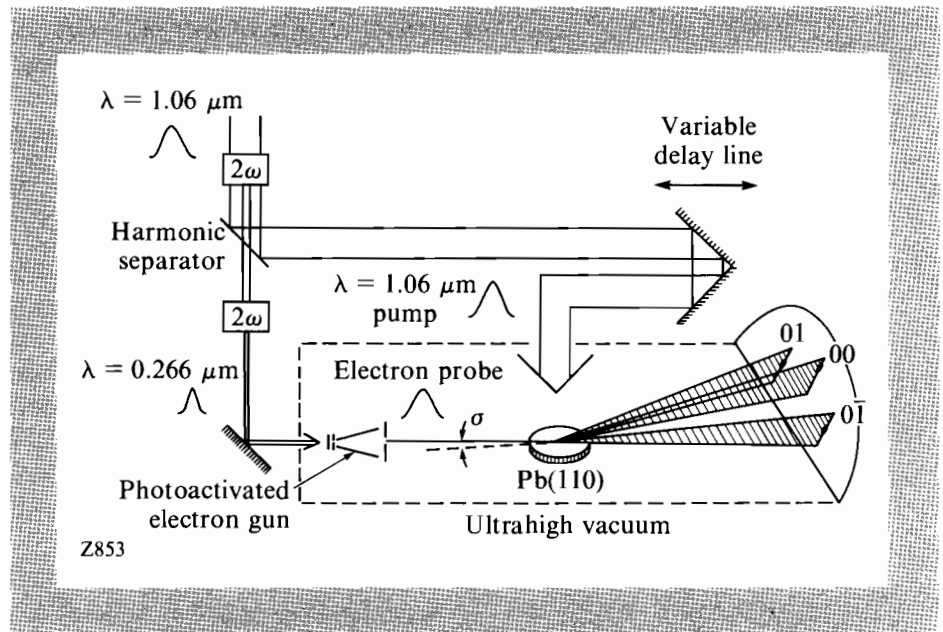


Fig. 48.21

Picosecond, time-resolved, reflection high-energy electron diffraction (RHEED). The laser pump and electron probe are well synchronized. The electron energy is 18.2 kV and the angle of incidence of the electron beam on the sample is  $\sim 3^\circ$ .

was demonstrated to be feasible.<sup>18</sup> Time-resolved RHEED patterns can also be obtained, giving information on the structure and temperature of the surface at various times relative to the arrival of the heating-laser pulse. Prior to experiments, the sample is cleaned by cycles of Ar ion bombardment followed by annealing. Sample cleanliness is checked by Auger electron spectroscopy.

We have recently used the technique of picosecond RHEED to time-resolve the surface-temperature rise induced by a  $\sim 170$ -ps laser pulse incident on Pb(110).<sup>18</sup> This work dealt with the fast temperature rise induced on a surface that was initially at room temperature and undergoes no phase transformation. For studying the time-resolved dynamics of the surface-disordering process, the sample is biased at a temperature close to the temperature at which the surface begins to disorder. For the work reported here, the sample is biased at 487 K. The picosecond laser-heating pulse raises the surface temperature from the initial bias level to temperatures ranging from below to above the surface-disorder temperature. The time-resolved intensity of the RHEED streaks is then obtained for given time delays between the laser-heating pulse and the electron probe pulse.

The picosecond RHEED pattern is amplified using a microchannel plate (MCP) proximity focused to a phosphor screen, the output of which is lens coupled onto a linear array detector. Quantitative analysis proceeds by taking line scans through the recorded RHEED streaks. A shutter is placed in the path of the heating-laser beam such that every other pulse interacts with the sample, producing RHEED patterns with and without laser heating. The associated line scans are sorted and averaged in separate memories of the computer. Data analysis consists of comparing the peak heights of the laser-heated and unheated scans and generating a graph of  $I/I_0$  versus time, where  $I$  and  $I_0$  are the intensities through the center of the considered RHEED streak

corresponding to the laser-heated surface and the nonheated surface, respectively. The RHEED pattern was studied to ensure that the shape of the streaks remains unchanged with temperature. Thus, the measured intensity of a RHEED streak is directly related to the number of electrons scattered into it. For the experiments reported here, the angle of incidence of the pulsed electron beam is  $\sim 3^\circ$ , resulting in a probe depth of  $\sim 3$  monolayers, and the electron beam is incident along the  $[1\bar{1}2]$  azimuth.

The modulation of the streak intensity caused by laser heating is related to the surface temperature through a calibration obtained by static heating. The sample is heated on a resistively heated stage and the intensity of a streak is recorded as a function of the surface temperature, measured by a thermocouple mounted on the surface of the sample. This yields the normalized RHEED streak intensity when the sample is heated from the bias temperature to a given temperature. Results of this measurement are shown in Fig. 48.22. This measurement provides the means by which we can assign a temperature to a particular nonvanishing RHEED streak intensity. For  $T \geq 540$  K, the elastically diffracted electron intensity becomes indistinguishable from the background, indicating the disordering of the probed surface layer. We thus define  $T_d = 540$  K as the temperature at which our probed layer is disordered.

The experimentally determined time-resolved modulation of the RHEED streak intensity for various laser fluences is shown in Fig. 48.23. This is to be compared with the solid line, which is the calculated intensity modulation obtained by converting the output of a solution of the one-dimensional heat-diffusion model to an intensity modulation using the calibration in Fig. 48.22. The model is given by the equation

$$C \frac{dT(z,t)}{dt} = K \frac{d^2T(z,t)}{dz^2} + I(1-R)\alpha e^{-\alpha z} f(t)^{-8.5},$$

where  $T(z, t)$  is the temperature profile at distance  $z$  normal to the surface ( $z = 0$ ),  $t$  is time,  $f(t)$  is the temporal dependence of the laser pulse, which is assumed Gaussian,  $C = 1.58 \times 10^6$  J/m<sup>3</sup> K is the heat capacity per unit volume,<sup>19</sup>  $K = 32.2$  W/m K is the thermal conductivity,<sup>19</sup>  $R = 0.81$  is the reflectivity,<sup>20</sup>  $\alpha = 7.05 \times 10^7$  m<sup>-1</sup> is the absorption coefficient,<sup>20</sup> and  $I$  is the peak laser intensity in W/cm<sup>2</sup>. For reference, the right side of the intensity-modulation graphs give the surface temperature obtained from the calibration in Fig. 48.22.

We next discuss the time-resolved heating and disordering results. In Figs. 48.23(a) and 48.23(b), the laser fluence is set so as to heat the surface to temperatures less than  $T_d$ . A solution of the heat-diffusion model for Figs. 48.23(a) and 48.23(b) gives peak surface temperatures of 523 K and 537 K, respectively. We then heated the surface with laser fluences sufficient to raise the surface temperature above  $T_d$  as shown in Figs. 48.23(c) and 48.23(d). A solution of the heat-diffusion model for the case in Fig. 48.23(c) indicates that the surface temperature is raised to  $\sim 558$  K, approximately 18 K above  $T_d$ . A solution of the model for the case in Fig. 48.23(d) predicts

Fig. 48.22

RHEED streak intensity versus sample temperature normalized to the streak intensity at the sample bias temperature of 487 K. The sample is heated on a resistively heated stage and the temperature is measured using a thermocouple attached to the surface. The location of the line scan across the diffraction pattern is the same as that for a pulsed laser heating experiment. A curve fit is made to the data and is used in conjunction with the heat-diffusion model to obtain the predicted time-resolved modulation of the RHEED streak intensity in Fig. 48.23. In the inset, the RHEED streak intensity is plotted on a logarithmic scale. The line fit includes data points up to that which maximizes the linear correlation.

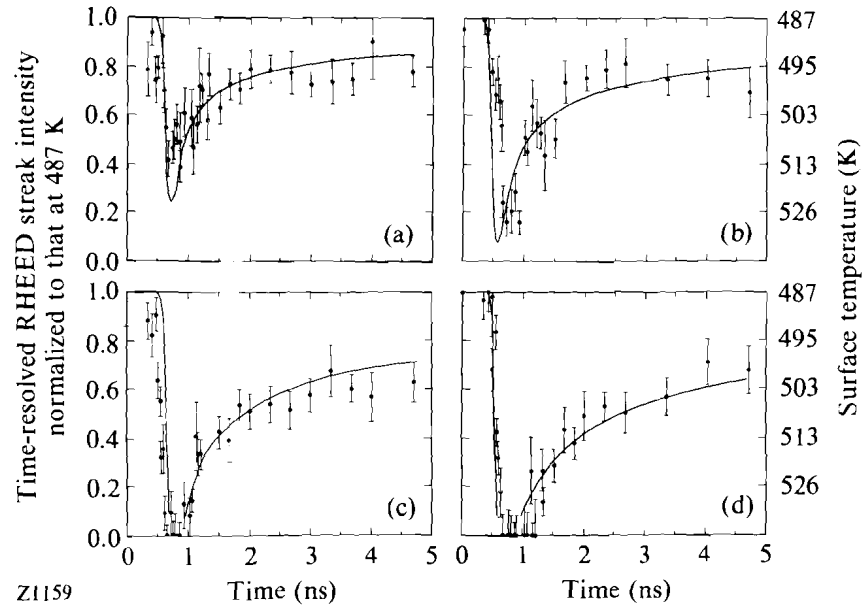
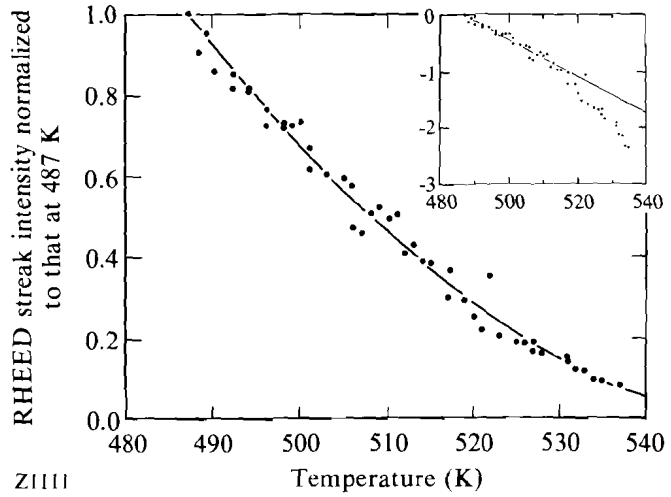


Fig. 48.23

Transient modulation of RHEED streak intensity and surface temperature on Pb(110) irradiated with Nd:YAG ( $\lambda = 1.06 \mu\text{m}$ ) laser pulses of varying peak intensities: (a)  $1.4 \times 10^7 \text{ W/cm}^2$ , 165-ps FWHM; (b)  $2.0 \times 10^7 \text{ W/cm}^2$ , 163-ps FWHM; (c)  $2.7 \times 10^7 \text{ W/cm}^2$ , 173-ps FWHM; (d)  $3.6 \times 10^7 \text{ W/cm}^2$ , 171-ps FWHM. In (c) and (d), the normalized streak intensity disappears for some time corresponding to a transient disordering of the probed surface layer. The reappearance of the streak intensity indicates the subsequent reordering of the surface.

a surface temperature rise to  $\sim 581$  K, approximately 41 K above  $T_d$ . The two fluences were chosen to explore the possible dependence of the disordering dynamics on overheating above  $T_d$ . In both cases, there exists some time where we are unable to detect RHEED streaks, corresponding to the elastically diffracted electrons, indicating that the probed surface region ( $\sim 3$  monolayers) is disordered. The time for which the streaks vanish depends on the level of overheating above  $T_d$  and is found to be  $\sim 200$  ps for Fig. 48.23(c) and  $\sim 500$  ps for Fig. 48.23(d). This is followed by the reappearance of the RHEED streaks as the surface cools and reorders. In all the graphs, the streak intensity is normalized to that at the bias temperature of 487 K. In Figs. 48.23(c) and 48.23(d), the results of the model are truncated since the static calibration, which allows us to convert the solution of the heat-diffusion model to an intensity modulation, could not detect the RHEED streaks above  $\sim 540$  K.

The error bars in Fig. 48.23 give the uncertainty of the streak intensity modulation and are mainly due to MCP noise. Other sources of errors in our measured intensity modulation include the spatial nonuniformity of the heating-laser profile on the surface, which is measured to be  $\pm 12\%$  across the surface, and the stability of our laser. Shot-to-shot laser fluctuations and long-term stability of the electron probe are compensated for by normalization and averaging. The heating-laser stability is regularly monitored during the experiment and is maintained to better than 10%. Our time-resolved measurements are the result of the convolution of the electron probing pulse with the actual temporal profile of the surface temperature. Such convolution effects, which are not included in our analysis, are most significant for times near the minimum of the normalized RHEED streak intensity where the rate of change of temperature with time is greatest. The absolute timing between the electron probe pulse and the laser-heating pulse is not experimentally determined. The temporal position of the theoretical streak-intensity modulations in Fig. 48.23 is set by minimizing the mean-square difference between the experimental results and the theory. For Figs. 48.23(a)–48.23(c), this minimization is performed for times between 1 and 2 ns, while for Fig. 48.23(d) it is performed between 1.3 and 3.3 ns. Taking the previous convolution effects into consideration, the sets in Figs. 48.23(a) and 48.23(b) show good agreement with the classical heat-diffusion model. In these sets, the laser fluence is kept below the fluence necessary for surface disordering.

The time-resolved modulation of the RHEED streak intensity for laser fluences above the surface disorder fluence again shows a good fit to that predicted from the classical heat-diffusion model. Observation of the actual growth of a disordered-surface region would result in a deviation between the experimentally determined, time-resolved intensity modulation and that predicted by classical heat diffusion. For example, a discrepancy in the time at which  $I/I_0$  vanishes could reflect the time required to nucleate and grow the disordered surface layers. However, with the present time resolution, this is not observed. This indicates that, although we have achieved laser-induced disordering of the surface, we are unable to observe the growth of the disordered layer with the present time resolution of our experiment. After

disordering, the normalized RHEED streaks reappear and their intensity agrees well with theoretical predictions. We conclude that the regrowth of crystalline order occurs in a time scale shorter than our time resolution. These results imply that the disordering and regrowth of the probed surface layer each occur in a time scale shorter than the pulse width of our electron probe.

In conclusion, using time-resolved RHEED, we have observed laser-induced surface disordering on Pb(110). Furthermore, this transformation is observed to be completely reversible within the time resolution of our experiment. This is significant since, previously, surface disordering has only been studied using conventional static surface probes. Here, we extend those measurements to heating and cooling rates of the order of  $10^{11}$  K/s. Finally, the actual growth of the disordered layer and the regrowth of surface order were not observed. We conclude from this that the times necessary to disorder and regrow the probed surface layer are each shorter than the pulse width of our electron probe ( $\sim 180$  ps).

#### ACKNOWLEDGMENT

This work was supported by the U.S. Department of Energy under contract No. DE-FG02-88ER45376. Additional support was provided by the Laser Fusion Feasibility Project at the Laboratory for Laser Energetics, which is sponsored by the New York State Energy Research and Development Authority and the University of Rochester. We gratefully acknowledge E. A. Murphy for her assistance with the experiments.

#### REFERENCES

1. G. Tammann, *Zeitschr. Phys. Chem.* **72**, 609 (1910).
2. J. W. M. Frenken and J. F. van der Veen, *Phys. Rev. Lett.* **54**, 134 (1985); J. W. M. Frenken, P. M. J. Maree, and J. F. van der Veen, *Phys. Rev. B* **34**, 7506 (1986).
3. B. Pluis *et al.*, *Phys. Rev. B* **40**, 1353 (1989); B. Pluis *et al.*, *Surf. Sci.* **239**, 265 (1990); B. Pluis, D. Frenkel, and J. F. van der Veen, *Surf. Sci.* **239**, 282 (1990).
4. U. Breuer, O. Knauff, and H. P. Bonzel, *Phys. Rev. B* **41**, 10848 (1990); *J. Vac. Sci. Technol. A* **8**, 2489 (1990).
5. K. C. Prince, U. Breuer, and H. P. Bonzel, *Phys. Rev. Lett.* **60**, 1146 (1988); U. Breuer *et al.*, *Surf. Sci.* **223**, 258 (1989).
6. E. A. Murphy, H. E. Elsayed-Ali, K. T. Park, J. Cao, and Y. Gao, *Phys. Rev. B* **43**, 12615 (1991).
7. P. H. Fuoss, L. J. Norton, and S. Brennan, *Phys. Rev. Lett.* **60**, 2046 (1988).
8. B. Pluis *et al.*, *Surf. Sci.* **222**, L845 (1989).
9. P. Stoltze, J. K. Nørskov, and U. Landman, *Phys. Rev. Lett.* **61**, 440 (1988); *Surf. Sci.* **220**, L693 (1989); P. Stoltze, *J. Chem. Phys.* **92**, 6306 (1990).

10. E. T. Chen, R. N. Barnett, and U. Landman, *Phys. Rev. B* **41**, 439 (1990).
11. F. Ercolessi *et al.*, *Surf. Sci.* **251/252**, 645 (1991).
12. J. F. Lutsko *et al.*, *Phys. Rev. B* **40**, 2841 (1989); D. Wolf *et al.*, *J. Mater. Res.* **5**, 286 (1990).
13. J. Mei and J. W. Davenport, to be published in *Physical Review B*.
14. See, for example, *Fundamentals of Beam-Solid Interactions and Transient Thermal Processing*, edited by M. J. Aziz, L. E. Rehn, and B. Stritzker (Materials Research Society, Pittsburgh, PA, 1988).
15. C. A. MacDonald, A. M. Malvezzi, and F. Spaepen, *J. Appl. Phys.* **65**, 129 (1989).
16. J. W. Christian, *The Theory of Transformations in Metals and Alloys*, 2nd ed. (Pergamon, Oxford, 1975).
17. R. Lipowsky and W. Speth, *Phys. Rev. B* **28**, 3983 (1983).
18. H. E. Elsayed-Ali and G. A. Mourou, *Appl. Phys. Lett.* **52**, 103 (1988); H. E. Elsayed-Ali and J. W. Herman, *Rev. Sci. Instrum.* **61**, 1636 (1990); H. E. Elsayed-Ali and J. W. Herman, *Appl. Phys. Lett.* **57**, 1508 (1990).
19. *Thermophysical Properties of Matter*, edited by Y. S. Toukougian (IFI/Plenum, New York, 1970), Vols. 1 and 4.
20. From  $R = [(n - 1)^2 + k^2]/[(n + 1)^2 + k^2]$  and  $\alpha = \frac{4\pi k}{\lambda}$  where  $n$  and  $k$  are the real and imaginary parts of the complex index of refraction. The values of  $n$  and  $k$  are obtained from an interpolation of the data in A. I. Golovashkin and G. P. Motulevich, *Sov. Phys. JETP* **26**, 881 (1968).

## 2.D Summer Research Program for High School Students

Ten students participated in the 8-week, summer of 1991 high school student research program at the Laboratory for Laser Energetics (LLE). The participants spent most of their time working on individual research projects, the results of which were presented at a symposium for their parents, teachers, and members of the LLE staff. Written reports of their work will be a permanent record of this summer's program. The students also participated in a series of seminars designed to teach them some of the concepts underlying the work performed at LLE, and they toured the Nuclear Structures Research Laboratory and the Strassenburg Planetarium. The components of the program are described in more detail in the following sections.

This is the third year LLE has had a summer program for high school students and the first that the program has been partially supported by the National Science Foundation (NSF). The goals of the program are to expose

students to state-of-the-art research in science and technology, and to incite them to pursue a career in these fields. We also hope that the enthusiasm generated by the program will be transferred to the students' peers.

The students, all of whom had completed their junior year, were selected from 60 outstanding applicants from 23 local high schools. Each student sent a letter of application, an NSF applicant form, and a copy of their transcript. In addition, each student was required to have a letter of recommendation from a science or math teacher. The applications were read and 20 of the applicants were invited for 25-minute interviews at LLE. The final ten were chosen after these intensive interviews.

### Projects

Each student, working under the direct supervision of one of the staff members of the laboratory, was assigned a research project. The students, their high schools, and their projects are listed in Table 48.III.

Table 48.III: High school students and their projects.

Student	High School	Project Title
Roger Clark	Penfield	UV Alignment Table
Ana Cotto	Benjamin Franklin	Neutron-yield Measurements with a Photomultiplier Tube
Robert Dick	Greece Arcadia	Scattering in Isotropic and Anisotropic Media
Jeffrey Dvorin	Brighton	A Better Approximation of the Diffusion Equation
Mark D. Forbes	Pittsford/Mendon	Design of a Photo-emissive, Electrostatically Focused Electron Gun
Elizabeth Randall	East	Spatial Resolution as a Function of Film Exposure
Franklin S. Turner	Rush-Henrietta	Analysis of Refractive Image Distortion
Helen Vayntrub	Brighton	Laser-Drilling Pinholes for X-ray Pinhole Cameras
Jeanne Yax	Nazareth	Does Perturbation Theory Accurately Describe Multiphoton Ionization?
Nora Yip	Webster	Wavefront Analysis Using Shearing Interferometry

E6074

#### Roger Clark–UV Alignment Table

The ultraviolet (UV) alignment table is a major component of the OMEGA laser system. The system incorporates a high-quality UV laser for alignment and beam-transport measurements. Roger's project involved a redesign, and subsequent installation, of the optical layout. He simplified the layout and significantly improved the UV-laser-beam quality.

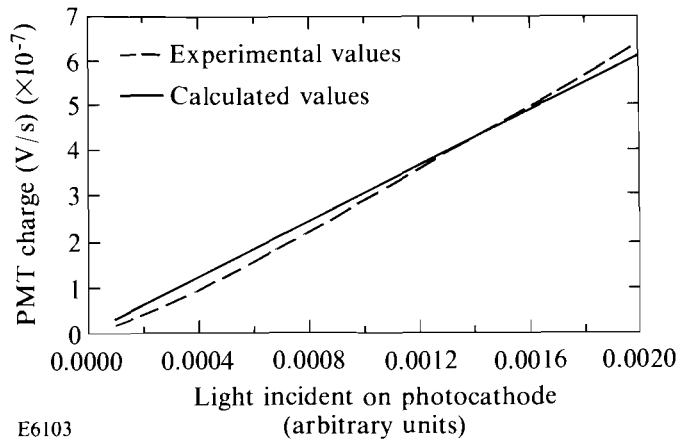
#### Ana Cotto–Neutron-yield Measurements with a Photomultiplier Tube

A photomultiplier tube (PMT) coupled to a scintillator can be used to measure the neutron yield from fusion experiments. A neutron strikes the

scintillator, producing a light pulse detected by the PMT. Ana's project was to calibrate the response of the PMT's as a function of their bias voltage and of the incident light flux. In this case a flashlamp light source was used as a reproducible source of x-rays to simulate the neutron source. Figure 48.24 shows a calibration of one of the PMT's at a bias voltage of -1600 V. The experimentally observed PMT charge produced as a function of the amount of incident light is plotted, along with calculated values.

Fig. 48.24

A comparison of the measured (dashed) and calculated (solid) PMT charge as a function of the amount of incident light.

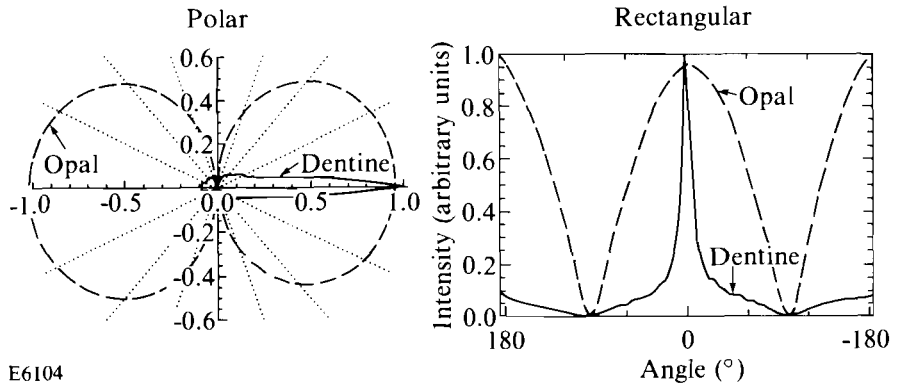


Robert Dick—Scattering in Isotropic and Anisotropic Media

The goal of this project was to measure the scattering of laser light in isotropic and anisotropic media: in particular, to study the scattering of light off dentine (dental tissue). A HeNe laser was incident on the material and the angular distribution of the absorption and scattering of the light was measured with a photodiode. Robert found that dentine has negligible absorption and exhibits strong forward scattering. The distribution of the scattered light strongly suggested that dentine has a crystalline structure. This is shown in Fig. 48.25, where the scattered light from dentine is compared to opal glass, an isotropic scatterer.

Fig. 48.25

Angular intensity distributions for light passing through opal glass and dentine.



#### Jeffrey Dvorin—A Better Approximation of the Diffusion Equation

In many of the computations performed at LLE to model the fusion experiments, the diffusion equation must be solved numerically. The solution depends on a tradeoff between accuracy and the length of time required for computation. Jeffrey's project involved testing new averaging schemes to be used in the solution of the diffusion equation. It was found that, in some cases, significant increases in computational speed could be achieved without sacrificing accuracy.

#### Mark D. Forbes—Design of a Photo-emissive, Electrostatically Focused Electron Gun

Electron optics are an important part of a number of experiments at LLE. A sophisticated electrostatic modeling code was used to design an electron gun with a photo-emissive electron source for use in an investigation of crystal structure and melting. Mark's goal was to produce the smallest possible beam diameter that would also have a small divergence over a 30–60-cm focusing distance.

#### Elizabeth Randall—Spatial Resolution as a Function of Film Exposure

An important question for many of the diagnostics used at LLE is how the photographic film used as the recording medium responds to different light fluences. In this project, the effect of the exposure on the spatial resolution of the film was measured. Two types of film were used: Kodak high-speed infrared 4143, and Kodak T-Max 400. Elizabeth found that as the fluence (from a 1-ns duration IR laser pulse), and hence the exposure, was increased, the spatial resolution of both films decreased.

#### Franklin S. Turner—Analysis of Refractive Image Distortion

In an experiment performed by C. Darrow<sup>1</sup> from Lawrence Livermore National Laboratory the image of a grid was projected through a plasma and the distortion of the image was measured at various distances, allowing a measure of the spatial profile of the plasma density. Franklin analyzed this data, showing that the refracted rays followed apparent straight-line trajectories, as expected. He also prepared the data for direct comparison with numerical simulations. A comparison of the measured and calculated contours of the refraction angle is shown in Fig. 48.26. Figures 48.26(a) and 48.26(b) show the experimental scattering angles in the horizontal and vertical plane, while Figs. 48.26(c) and 48.26(d) show the results of the numerical simulations.

#### Helen Vayntrub—Laser-drilling Pinholes for X-ray Pinhole Cameras

X-ray pinhole cameras are one of the important diagnostics used at LLE. They are used to observe the size of the compressed pellets. For high spatial resolution, pinholes of 2–10- $\mu\text{m}$  diam are required. The pinholes are produced by tightly focusing a laser beam onto a thin metal foil, and then drilling a hole. A high-quality laser beam is required to make the best pinholes. Helen studied the size of the hole produced as a function of the peak laser intensity.

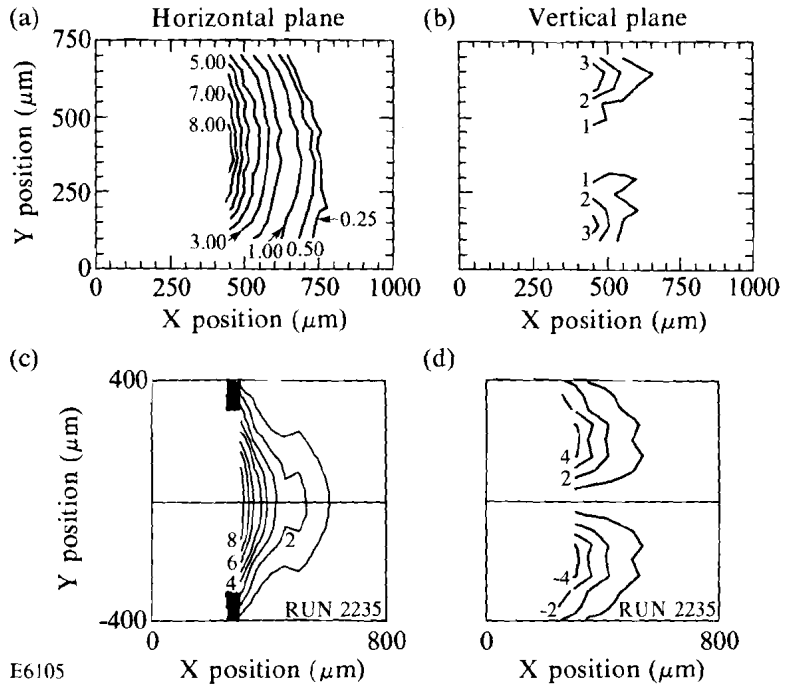


Fig. 48.26  
 Contours of the refraction angles in degrees. (a) Contour plot of the horizontal refraction angle  $\theta_x$ . (b) Contour plot of the vertical refraction angle  $\theta_y$ . The contours on the bottom of the graph are negative, and the ones on top are positive. Predicted refraction-angle contours for the plasma, as calculated by *SAGE*, are shown in Figs. 48.26(c) and 48.26(d). (c) Horizontal refraction angle  $\theta_x$ . (d) Vertical refraction angle  $\theta_y$ .

Jeanne Yax—Does Perturbation Theory Accurately Describe Multiphoton Ionization?

The multiphoton ionization experiments performed by many different experimental groups were compared. Jeanne searched the published literature, the data presented was digitized, and the slope of the number of ions detected versus peak laser intensity was measured. In perturbation theory, this slope should be equal to the minimum number of photons required for ionization. This was found to be true for the lowest charge states, except in the experiments that used the fewest optical cycles in their ionizing laser pulse.

Nora Yip—Wavefront Analysis Using Shearing Interferometry

The quality of optical components can be tested using interferometry. The collimation of a laser beam can also be measured. In this project, Nora compared shearing interferometry with two-beam interferometry. The advantages of a shearing interferometer are: it does not require a separate reference beam, and quick tests of phase information can be obtained with moderate resolution. In many cases it was found that a measurement of phase information from a shearing interferometer agreed with the higher-resolution phase information obtained from a two-beam interferometer.

Symposium

The summer ended with a research symposium given by the students. It was attended by parents, teachers, and members of the LLE staff. The students wrote and presented an overall introduction to the presentations,

describing the work performed at LLE this summer and the relationships among their projects. Each student made a 10–15-min presentation about their research work, and answered questions. Finally, a group conclusion summarizing the projects was presented. The students also prepared a 10–20-page written summary of their work. These papers will be compiled into a report that will be available to any interested parties.

### **Conclusions**

In the third year of LLE's summer high school research program, ten students from local high schools spent eight weeks at LLE working on research projects. These projects are part of the ongoing research at the laboratory, so the students were immersed in a real research environment, with all of its attendant frustration and satisfaction.

### **ACKNOWLEDGMENT**

This program was supported in part by the National Science Foundation under contract No. RCD-9055084.

### **REFERENCES**

1. C. Darrow *et al.*, *J. Appl. Phys.* **67**, 3630 (1990).

## Section 3

# NATIONAL LASER USERS FACILITY NEWS

NLUF activity for the fourth quarter of FY91 was centered around experiments conducted on GDL. These were done by groups from the University of Illinois (UI) and from the National Institute of Standards and Testing (NIST). Groups from the University of Maryland and from the University of Florida visited to discuss future scheduling of experiments on OMEGA.

The Air Force Office of Scientific Research is funding an experiment on GDL being conducted by UI. This experiment is being done in collaboration with LLE scientists and is studying the change in the characteristics of metals caused by a laser-generated shock wave. The samples are prepared by the Department of Materials Science and Engineering at UI, irradiated with the GDL laser, and returned to UI for detailed micro-analysis. Other diagnostics for this experiment are fielded by both LLE and UI scientists.

**J. Reader** from NIST has set up a high-resolution XUV spectrograph to measure the line radiation from laser-produced plasmas. The spectrograph is a McPhearson grazing incidence XUV spectrograph. The target chamber is attached to the instrument and an external lens is used to focus the laser onto the target. The spectra are recorded on Kodak 101 glass plates that have been pre-exposed with a calibration spectrum. This instrument has provided some of the highest resolution measurements of line radiation from laser-produced plasmas to date. It is expected that there will be at least one more set of exposures taken before the instrument is returned to NIST.

On separate occasions, groups from the University of Maryland and the University of Florida visited the laboratory to discuss future OMEGA experiments. Both experiments will use noble-gas-seeded targets to study the line radiation from hot, dense matter. D<sub>2</sub> targets seeded with neon are planned for **H. Griem's** group from the University of Maryland. Time-dependent and time-integrated spectra are to be recorded and analyzed. D<sub>2</sub> targets seeded with argon are being planned for **C. Hooper's** group from the University of Florida. Time-resolved spectra will be recorded with two separate crystal spectrographs. Both groups are waiting for the targets to be constructed before experiments can be scheduled for OMEGA.

#### ACKNOWLEDGMENT

This work was supported by the U.S. Department of Energy Office of Inertial Confinement Fusion under agreement No. DE-FC03-85DP40200.

## Section 4

# LASER SYSTEM REPORT

### 4.A GDL Facility Report

There was a total of 391 GDL shots during the fourth quarter of FY91. The target shots were in support of NLUF users from the University of Illinois and the National Institute of Standards and Testing. The laser experimental shots were used to measure Bessel-beam propagation, IR film MTF curves, and a project in support of the LLE high school summer student program.

The shot summary for the GDL laser this quarter is as follows:

Laser system	62
Laser calibration	24
Laser experiments	101
Target	<u>204</u>
TOTAL	391

### 4.B OMEGA Facility Report

There was a total of 353 OMEGA shots during the fourth quarter of FY91. The majority of shots were devoted to the driver line. The primary activity for this quarter was the final installation of the pulse-shaping apparatus. Pulses from the long-pulse regenerative amplifier, with widths set to 750-ps FWHM to approximate the output of the previous OMEGA oscillator, are now injected into the OMEGA driver line and from there into the remainder of the power-amplifier chain. This system is now an integral part of the OMEGA laser system.

The system is now being readied for target shots on D<sub>2</sub> and DT implosion targets. The 11 target shots were used to check system timing, target diagnostics, and laser status. The OMEGA transport integrating sphere (OTIS) has been rebuilt and is used to characterize the transport losses from the conversion crystals to the center of the target chamber. Target shots will start during the first quarter of FY92 and are to continue until the October 1992 shutdown of the OMEGA laser.

The shot summary for OMEGA this quarter is as follows:

Software test	8
Driver	263
Laser	71
Target	<u>11</u>
TOTAL	353

#### ACKNOWLEDGMENT

This work was supported by the U.S. Department of Energy Office of Inertial Confinement Fusion under agreement No. DE-FC03-85DP40200 and by the Laser Fusion Feasibility Project at the Laboratory for Laser Energetics, which is sponsored by the New York State Energy Research and Development Authority and the University of Rochester.



# PUBLICATIONS AND CONFERENCE PRESENTATIONS

## Publications

S. Alexandrou, R. Sobolewski, H. Nakano, B. C. Tousley, and T. Y. Hsiang, "Picosecond Characterization of Bent Coplanar Waveguides," *IEEE Microwave and Guided Wave Letters* **1**, 236–238 (1991).

E. M. Epperlein, G. J. Rickard, and A. R. Bell, "A Code for the Solution of the Vlasov-Fokker-Planck Equation in 1-D or 2-D," *Comput. Phys. Commun.* **52**, 7–13 (1991).

D. Golini and S. D. Jacobs, "Physics of Loose Abrasive Microgrinding," *Appl. Opt.* **30**, 2761–2777 (1991).

T. Gong, P. Mertz, W. L. Nighan, Jr., and P. M. Fauchet, "Femtosecond Refractive-Index Spectral Hole Burning in Intrinsic and Doped GaAs," *Appl. Phys. Lett.* **59**, 721–723 (1991).

T. Gong, P. M. Fauchet, J. F. Young, and P. J. Kelly, "Femtosecond Gain Dynamics Due to Initial Thermalization of Hot Carriers Injected at 2 eV in GaAs," *Phys. Rev. B* **44**, 6542–6545 (1991).

M. J. Guardalben, A. Bevin, K. L. Marshall, A. W. Schmid, and F. Kreuzer, "1053-nm High-Field Effect in Monomeric and Polymeric Conjugated Systems," in *Natl. Inst. Stand. Technol. (U.S.), Spec. Publ. 775* (U.S. Government Printing Office, Washington, DC, 1989), pp. 462–469 (1991).

J. D. Kilkenny, P. M. Bell, B. A. Hammel, R. L. Hanks, O. L. Landen, T. E. McEwan, D. S. Montgomery, R. E. Turner, J. D. Wiedwald, and D. K.

Bradley, "Sub 100 psec X-Ray Gating Cameras for ICF Imaging Applications," in *19th International Congress on High-Speed Photography and Photonics* (SPIE, Bellingham, WA, 1990), Vol. 1358, pp. 117–133 (1991).

S. Krishnamurthy and S.-H. Chen, "New Thermotropic Chiral Nematic Copolymers. 2. A Study of Helical Sense and Twisting Power Based on Copolymers Containing (S)-(-)-1-Phenylethyl Alcohol and (R)-(-)-Methyl Mandelate," *Macromolecules* **24**, 3481–3484 (1991).

S. Krishnamurthy and S. H. Chen, "Facilitating the Formation of the Grandjean Texture in Thermotropic Chiral Nematic Side-Chain Copolymers via Modulation of Backbone Flexibility," *Macromolecules* **24**, 4472–4474 (1991).

G. G. Luther, C. J. McKinstrie, and A. L. Gaeta, "Transverse Modulational Instability of Counterpropagating Light Waves," in *OSA Proceedings on Nonlinear Dynamics in Optical Systems*, edited by N. B. Abraham, E. M. Garmire, and P. Mandel (Optical Society of America, Washington, DC, 1991), Vol. 7, pp. 205–209 (1991).

M. D. Skeldon, M. S. Jin, D. J. Smith, and S. T. Bui, "Performance of Longitudinal Mode KD\*P Pockels Cells with Transparent Conductive Coatings," in *Solid State Lasers II* (SPIE, Bellingham, WA, 1991), Vol. 1410, pp. 116–124 (1991).

R. Sobolewski, "Applications of High- $T_c$  Superconductors in Optoelectronics," in *Infrared and Optoelectronic Materials and Devices* (SPIE, Bellingham, WA, 1991), Vol. 1512, pp. 14–27.

J. M. Wallace and E. M. Epperlein, "Weibel Instability with Constant Driving Source," *Phys. Fluids B* **3**, 1579–1586 (1991).

## Forthcoming Publications

J. W. Herman and H. E. Elsayed-Ali, "Time-Resolved Study of Surface Disorder of Pb(110)," to be published in *Physical Review Letters*.

A. Honig, N. Alexander, Q. Fan, R. Q. Gram, and H. Kim, "Absence of Molecular Deuterium Dissociation During Room-Temperature Permeation into Polystyrene ICF Target Shells," to be published in the *Journal of Vacuum Science and Technology A*.

R. H. Hwang-Schweitzer, R. S. Knox, P. B. Gibbs, and J. Biggins, "Fluorescence Studies of Photoregulation in the Chrysophyte *Ochromonas danica*," to be published in the *Journal of Luminescence*.

J. H. Kelly, "Instrumentation Integration in Large Systems: the OMEGA Laser Upgrade at the University of Rochester as an Example," to be published in the *Proceedings of the OSA 1991 Annual Meeting*, San Jose, CA, 3–8 November 1991 (invited paper).

J. H. Kelly, M. Shoup III, M. D. Skeldon, and S. T. Bui, "Design and Energy Characterization of a Multi-Segment Glass Disk Amplifier," to be published

in the *Proceedings of the SPIE's OE/LASE '91 Symposium*, Los Angeles, CA, 20–25 January 1991.

J. H. Kelly, M. J. Shoup III, M. M. Tedrow, C. D. Kiikka, T. J. Kessler, S. A. Kumpan, A. W. Schmid, M. D. Skeldon, and D. J. Smith, “The 30 kJ OMEGA Upgrade at the University of Rochester, a Flexible, High-Performance Nd:Glass Driver,” to be published in the *Proceedings of the IAEA Technical Committee Meeting on Drivers for Inertial Confinement Fusion*, Osaka, Japan, 15–19 April 1991.

H. Kim, B. Yaakobi, J. M. Soures, and P.-C. Cheng, “Laser-Produced Plasma as a Source for X-Ray Microscopy,” to be published in *X-Ray Microscopy III*, edited by A. Michette *et al.* (Springer-Verlag, New York).

H. Kim, R. Q. Gram, M. D. Wittman, C. Immesoete, R. S. Craxton, N. Sampat, S. Swales, G. Pien, and J. M. Soures, “Uniform Liquid Fuel Layer Produced in a Cryogenic Target by a Time-Dependent Thermal Gradient,” to be published in the *Proceedings of the Seventh Target Fabrication Specialists Meeting*, Livermore, CA, 25–29 September 1989.

H. G. Kim, C. K. Immesoete, and S. Scarantino, “Computer-Assisted Microballoon Selection for Inertial Fusion Targets,” to be published in the *Proceedings of the Seventh Target Fabrication Specialists Meeting*, Livermore, CA, 25–29 September 1989.

J. C. Lambropoulos and S.-S. Hwang, “Film Thermal Conductivity and Laser Damage Resistance of Optical Thin Films,” to be published in the *Proceedings of a Symposium on Electro-Optics and Non-Linear Optics, 1st International Congress on Ceramic Science and Technology*, Anaheim, CA, 1–3 November 1989.

Y. Lin, W. Seka, J. H. Eberly, H. Huang, and D. L. Brown, “Experimental Investigation of Bessel Beam Characteristics,” to be published in *Applied Optics (Lasers and Photonics)*.

G. G. Luther and C. J. McKinstrie, “The Transverse Modulational Instability of Counterpropagating Light Waves,” to be published in the *Journal of the Optical Society of America B*.

R. L. McCrory, “Laser-Driven ICF Experiments,” to be published in *Nuclear Fusion by Inertial Confinement* (CRC Press).

R. L. McCrory and C. P. Verdon, “Computer Modeling and Simulation in Inertial Confinement Fusion,” to be published in *Il Nuovo Cimento*.

R. L. McCrory, J. M. Soures, J. Knauer, S. Letzring, F. J. Marshall, S. Skupsky, W. Seka, C. Verdon, D. Bradley, R. S. Craxton, J. Delettrez, R. Epstein, P. Jaanimagi, R. Keck, T. Kessler, H. Kim, R. Kremens, P. W. McKenty, R. Short, and B. Yaakobi, “Direct-Drive Implosion Experiments at the Laboratory for Laser Energetics,” to be published in the *Proceedings of the Thirteenth International Conference on Plasma Physics and Controlled Nuclear Fusion Research*, Washington, DC, 1–6 October 1990.

R. L. McCrory, J. M. Soures, J. P. Knauer, S. A. Letzring, F. J. Marshall, S. Skupsky, W. D. Seka, C. P. Verdon, D. K. Bradley, R. S. Craxton, J. A.

Delettrez, R. Epstein, P. A. Jaanimagi, R. L. Keck, T. J. Kessler, H. Kim, R. L. Kremens, P. W. McKenty, R. W. Short, and B. Yaakobi, "Short-Wavelength-Laser Requirements for Direct-Drive Ignition and Gain," to be published in the *Proceedings of the IAEA Technical Committee Meeting on Drivers for Inertial Confinement Fusion*, Osaka, Japan, 15–19 April 1991, and in *Laser and Particle Beams*.

C. J. McKinstrie and M. Yu, "The Role of Ion Momentum in Stimulated Raman Scattering," to be published in *Physics of Fluids B*.

C. J. McKinstrie and R. Bingham, "Stimulated Raman Forward Scattering and the Relativistic Modulational Instability of Light Waves in Rarefied Plasma," to be published in *Physics of Fluids B*.

D. D. Meyerhofer, S. Augst, C. I. Moore, and J. Peatross, "Angular Distribution of High-Order Harmonics Generated in the Tunneling Regime," to be published in the *Proceedings of SPIE's 36th International Symposium on Optical Applied Science and Engineering and Scanning Microscopy Instrumentation*, San Diego, CA, 21–26 July 1991 (invited paper).

E. A. Murphy, H. E. Elsayed-Ali, K. T. Park, J. Cao, and Y. Gao, "Temperature Dependent Anisotropy of Pb(100) Surface Structure," to be published in *Physical Review B*.

S. Papernov, L. Pedulla, V. Zandy, A. W. Schmid, and P. Resnick, "Perfluorinated Copolymer Coatings for High-Power Laser Applications," to be published in *Applied Physics Letters*.

D. Y. Park, W. Seka, Y. Lin, and D. L. Brown, "Operational Characteristics of an Imaging, Unstable Ring Resonator Using Nd:YLF as Active Medium," to be published in the *Proceedings of the Ninth Workshop on Laser Interaction and Related Plasma Phenomena*, Monterey, CA, 6–10 November 1989.

J. Peatross, M. V. Fedorov, and D. D. Meyerhofer, "Laser Temporal and Spatial Effects on Ionization Suppression," to be published in the *Journal of the Optical Society B*.

J. K. Samarabandu, R. Acharya, C. D. Edirisinghe, P. C. Cheng, H. Kim, T. H. Lin, R. G. Summers, and C. E. Musial, "Analysis of Multi-Dimensional Confocal Images," to be published in the *Proceedings of the SPIE Symposium "Biomedical Imaging"*, San Diego, CA, 24 February 1991.

W. D. Seka, R. S. Craxton, R. E. Bahr, D. L. Brown, D. K. Bradley, P. A. Jaanimagi, B. Yaakobi, and R. Epstein, "Production and Characterization of Hot, Long-Scale-Length Laser Plasmas," to be published in *Physics of Fluids*.

L. J. Shaw-Klein, T. K. Hatwar, S. J. Burns, S. D. Jacobs, and J. C. Lambropoulos, "Anisotropic Thermal Conductivity of Rare Earth-Transition Metal Thin Films," to be published in the *Journal of Materials Research*.

M. D. Skeldon, R. S. Craxton, T. Kessler, W. Seka, R. Short, S. Skupsky, and J. M. Soures, "Efficient Harmonic Generation with a Broadband Laser," to be published in *IEEE Journal of Quantum Electronics*.

J. M. Soures, "Solid State Lasers," to be published in *Nuclear Fusion by Inertial Confinement*, edited by G. Velarde, Y. Ronen, and J. M. Martinez-Val.

J. M. Soures, "High-Technology Advances from LLE Research," to be published in the *Rochester Business Profiles Journal*.

J. M. Soures, "The OMEGA Upgrade Laser Facility for Direct-Drive Experiments," to be published in the *Proceedings of the Fusion Power Associates Annual Meeting and Symposium*, Princeton, NJ, 25–26 June 1991, and in the *Journal of Fusion Energy* (Plenum Press).

J. M. Soures, R. L. McCrory, T. R. Boehly, R. S. Craxton, S. D. Jacobs, J. H. Kelly, T. J. Kessler, J. P. Knauer, R. L. Kremens, S. A. Kumpan, S. A. Letzring, W. D. Seka, R. W. Short, M. D. Skeldon, S. Skupsky, and C. P. Verdon, "OMEGA Upgrade Laser for Direct-Drive Target Experiments," to be published in the *Proceedings of the IAEA Technical Committee Meeting on Drivers for Inertial Confinement Fusion*, Osaka, Japan, 15–19 April 1991, and in *Laser and Particle Beams*.

M. D. Wittman, D. Malacara, and H.-J. Kong, "High-Precision Characterization of Gas-Filled Shells," to be published in the *Proceedings of SPIE's 1991 International Symposium on Optical Applied Science and Engineering*, San Diego, CA, 21–26 July 1991.

B. Yaakobi, R. Epstein, and F. J. Marshall, "Diagnosis of Laser Compressed Shells Based on Absorption of Core Radiation," to be published in *Physical Review*.

X. Zhou and T. Y. Hsiang, "EMCUR: An Ensemble Monte Carlo Program for III-V Compound Semiconductor Device Modeling and Simulation," to be published in *IEEE Transactions on Computer-Aided Design*.

## Conference Presentations

The following presentations were made at the Seventh International Conference on Hot Carriers in Semiconductors (HC/S-7), Nara, Japan, 1–5 July 1991:

P. M. Fauchet, T. Gong, P. J. Kelly, and J. F. Young, "Femtosecond Gain Dynamics in Thin GaAs Films."

T. Gong and P. M. Fauchet, "Femtosecond Carrier Scattering Processes in the Presence of a Cold Plasma."

---

H. Kim, "Investigation of Inertial-Fusion Targets by Confocal Microscopy and X-ray Microtomography," presented at 3D Microscopies '91, an International Conference on Three Dimensional Imaging, Taipei, Taiwan, 10–12 July 1991 (invited paper).

---

The following presentations were made at the SPIE International Symposium on Optical Applied Science and Engineering and Scanning Microscopy Instrumentation, San Diego, CA, 21–26 July 1991:

H. Kim, P.-C. Cheng, M. D. Wittman, J. M. Soures, R. S. Acharya, T. H. Lin, and J. Samarabandu, "Characterization of Inertial Fusion Targets with Confocal Light Microscopy."

D. D. Meyerhofer, S. Augst, C. I. Moore, and J. Peatross, "Angular Distribution of High-Order Harmonics Generated in the Tunneling Regime," (invited paper).

M. D. Wittman, D. Malacara, and H.-J. Kong, "High-Precision Characterization of Gas-Filled Shells."

---

L. J. Shaw-Klein, T. K. Hatwar, S. J. Burns, S. D. Jacobs, and J. C. Lambropoulos, "Thermal Conductivity of Amorphous Rare Earth-Transition Metal Thin Films for Magneto-Optic Recording," presented at the International Workshop on Science and Technology of Thin Films for the 21st Century, Evanston, IL, 28 July–2 August 1991.

---

The following presentations were made at the Eighth Target Fabrication Specialists Meeting, Albuquerque, NM, 23–26 September 1991:

H. Kim, S. G. Noyes, and J. M. Soures, "Fabrication of Polystyrene Shells Using the Microencapsulation Technique."

H. Kim, J. M. Soures, and P.-C. Cheng, "Investigation of Inertial Fusion Target by Confocal Microscopy and X-Ray Microtomography."

M. Wittman, R. Gram, H. Kim, and J. M. Soures, "Measurement of the Permeation Rate of Plastic Shells Using a Newly Developed Fabry-Perot Interferometer."

M. D. Wittman, A. S. Chow, and H. Kim, "Analysis of Newton Rings in ICF Targets Using Narrow-Band Illumination."

---

R. Sobolewski, "Prospects for High- $T_c$  Superconducting Optoelectronics," presented at the Conference on Superconductivity and Applications, Buffalo, NY, 24–26 September 1991.

#### ACKNOWLEDGMENT

The work described in this volume includes current research at the Laboratory for Laser Energetics, which is supported by New York State Energy Research and Development Authority, the University of Rochester, the U.S. Department of Energy Office of Inertial Confinement Fusion under agreement No. DE-FC03-85DP40200, and other agencies.

UNIVERSITY OF  
ROCHESTER